

1
2 **Quality-Controlled Upper-Air Sounding Dataset for DYNAMO/CINDY/AMIE:**
3 **Development and Corrections**

4
5 Paul E. Ciesielski¹, Hungjui Yu¹, Richard H. Johnson¹,
6 Kunio Yoneyama, Masaki Katsumata²,
7 Charles N. Long³,
8 Junhong Wang^{4,5},

9 Scot M. Loehrer, Kathryn Young, Steven F. Williams, William Brown⁵,
10 John Braun, Teresa Van Hove⁶

11
12
13 ¹ Department of Atmospheric Science, Colorado State University, Fort Collins, CO

14
15 ² Japanese Agency for Marine-Earth Science and Technology

16 ³ Pacific Northwest National Laboratory

17 ⁴ Department of Atmospheric and Environmental Sciences, University at Albany, State
18 University of New York

19 ⁵ National Center for Atmospheric Research

20 ⁶ University Corporation for Atmospheric Research

21
22 Submitted to Journal of Atmospheric and Oceanic Technology

23
24 August 2013

25
26 Corresponding author address: Paul E. Ciesielski, Department of Atmospheric Science,
27 Colorado State University, Fort Collins, CO 80523.

28
29 E-mail: paulc@atmos.colostate.edu

41

Abstract

42 The upper-air sounding network for DYNAMO (Dynamics of the Madden-Julian
43 Oscillation or MJO) has provided an unprecedented set of observations for studying the
44 MJO over the Indian Ocean (IO) where coupling of this oscillation with deep convection
45 first occurs. With 72 rawinsonde sites and dropsonde data from 13 aircraft missions, the
46 sonde network covers the tropics from Eastern African to the West Pacific. In total nearly
47 26,000 sondes were collected from this network during the experiment's 6-month
48 extended observing period (from October 2011 to March 2012). Slightly more than half
49 of the sondes, collected from 33 sites, are at high vertical resolution. Rigorous post-field
50 phase processing of the sonde data included several levels of quality checks and a variety
51 of corrections which address a number of issues (e.g., daytime dry bias, baseline surface
52 data errors, ship deck-heating effects, artificial dry spikes in slow-ascent sondes).

53 Because of the importance of an accurate description of the moisture field in meeting
54 the scientific goals of the experiment, particular attention is given to humidity correction
55 and its validation. The humidity corrections, though small relative to some previous field
56 campaigns, produced high fidelity moisture analyses in which sonde precipitable water
57 compared well with independent estimates. An assessment of model operational analyses
58 moisture using corrected sonde data shows an overall good agreement with the exception
59 at upper-levels where model moisture and clouds are more abundant than the sounding
60 data would indicate.

61

62

63

64 **Introduction**

65 Due to limitations in our basic understanding of and ability to predict the MJO,
66 particularly its initiation, a field campaign was recently conducted in the Indian Ocean
67 (IO) region during the period October 2011 to March 2012 (Yoneyama et al. 2013). The
68 experiment was comprised of three principal components: DYNAMO (Dynamics of the
69 MJO); CINDY2011 (Cooperative Indian Ocean experiment on intraseasonal variability in
70 the Year 2011); and AMIE (Atmospheric Radiation Measurement (ARM) MJO
71 Investigation Experiment). Hereafter, the collective field campaign effort will be referred
72 to as DYNAMO.

73 Because of the large-scale nature of the MJO, an enhanced upper-air sounding
74 network was established over the IO region (Fig. 1) which extended zonally from eastern
75 Africa to the West Pacific. Observations from this network will allow the study of MJO
76 initiation over the IO, where its deep convection signal is first observed, and its
77 subsequent evolution over the maritime continent and West Pacific warm pool region. A
78 primary component of this enhanced network were six core sounding sites in central IO
79 which formed two quadrilateral sounding arrays, one north and one south of the equator.
80 These two arrays will provide the observations necessary for diagnostic studies of heat
81 and moisture budgets from which the properties of convection can be inferred (Yanai et
82 al. 1973). In addition, the data allow for the computation of advective properties of heat
83 and moisture to force cloud-resolving models and single-column models, which aids in
84 the improvement of parameterization schemes (Wu et al. 2000).

85 Building on the success of past tropical field campaigns, most notably the Global
86 Atmospheric Research Program Atlantic Tropical Experiment (GATE) in 1973 (Kuettner

87 et al. 1974) and the Tropical Ocean Global Atmosphere Coupled Ocean-Atmosphere
88 Response Experiment (TOGA COARE) in 1992-93 (Webster and Lukas 1992),
89 DYNAMO provides scientifically important observations over data-sparse regions of our
90 planet. In addition to the important budget applications cited above, these sounding
91 networks provide the observations needed to: describe environmental conditions that
92 provide a context for validating and understanding other observations (radar, satellite,
93 etc.); initialize models for reanalyses and case studies; and validate models. In particular,
94 high vertical resolution (hi-res) DYNAMO sounding observations will be instrumental in
95 achieving the stated goal of determining the mechanisms by which the troposphere is
96 moistened in the initiation stage of the MJO.

97 Considering the wide use of the sounding dataset and the requirement for high-quality
98 observations to meet the experimental goals, a special effort was undertaken to create the
99 “best possible” set of sounding observations. The purpose of this paper is to document
100 the performance and characteristics of the DYNAMO upper-air sounding network
101 (section 2) and to describe the quality-control (QC) procedures (Section 3) and
102 corrections to the sonde data (Section 4). Our confidence in the accuracy of the sonde
103 humidity observations shown in Sections 4 and 5, allows us to use them as a tool to
104 evaluate the reliability of some satellite and model-based moisture products (Section 5).
105 Summary comments are provided in Section 6.

106 **2. Upper-air network overview and other data sources**

107 *a) Sonde inventory*

108 While data collection for a few DYNAMO sites began as early as late September
109 2011, most sites began observations around 1 October 2011. This date marked the formal

beginning of three noteworthy observing periods for the experiment which are summarized in Table 1. In general, the best data coverage for both arrays occurred during the Special Observing Period (SOP) from early October through the end of November during which time two robust MJOs passed over the network (Johnson and Ciesielski 2013). A visual inventory of the six core sites is shown in Fig. 2. From this plot we note that the Southern Sounding Array (SSA; bottom four panels) was configured to achieve 8/day sondes in a quadrilateral network through the end of the SOP after which it was triangular shaped with 4/day sondes when the *R/V Mirai* departed and the *R/V Revelle* was on site. On the other hand, the Northern Sounding Array (NSA; top four panels) was configured as a quadrilateral through 15 December when the *Revelle* was on site and triangular when not. The typical launch frequency at Malé and Colombo was 4/day during the SOP, however after 05 December the frequency at Colombo was reduced to 1/day.

Sounding operations at 11 sites in the DYNAMO domain (including the six core sites) were enhanced either by increasing sonde frequency above normal operational frequency or establishing operations where none previously existed. Hi-res data were collected for these 11 sites which are labeled with their station names in Fig. 1 and highlighted in bold in Table 2. Two of the enhanced sites at Diego Garcia and *R/V Revelle* deployed a National Center for Atmospheric Research (NCAR) Integrated Sounding Systems (ISS) which included a surface meteorological (SMET) station, a 915-MHz wind profiler, a Global Positioning System (GPS) Advanced Upper-Air Sounding (GAUS) system, and a ground-based GPS receiver for computation of total column Precipitable Water (PW). As part of the ISS system at Diego Garcia, a Radio Acoustic

133 Sounding System (RASS) was also deployed to retrieve virtual temperature profiles up to
134 about 1 km.

135 In addition to the 11 enhanced sites, 45 operational sites in the large-scale of
136 DYNAMO were identified prior to experiment as important to providing a broader-scale
137 context for the core DYNAMO observations. An effort was made to obtain hi-res data
138 from these priority sounding sites (PSS) by sending requests to many of the countries
139 involved. While these requests met with limited success, in the end hi-res data were
140 obtained from 21 of these sites (identified with a filled black dot in Fig. 1). Station
141 information for sites in which high vertical resolution data were collected is listed in
142 Table 2 including dropsondes from 13 National Atmospheric and Oceanic Administration
143 (NOAA) P3 aircraft missions. Two of the sites listed in Table 2, Pontianak and Sipora,
144 represent part of an enhanced sonde network for the Hydrometeorological ARray for Isv-
145 Monsoon AUtomonitoring (HARIMAU) project (Yamanaka et al. 2008).

146 For the remaining 24 PSS without hi-res data (white dots in Fig. 1), an effort was
147 made to obtain a complete record of their Global Telecommunication System (GTS)-
148 resolution data by utilizing the University of Wyoming sonde data archive
149 (<http://weather.uwyo.edu/upperair/sounding.html>). Finally, during the field phase of the
150 experiment GTS resolution data were collected for an additional 16 non-PSS in the
151 DYNAMO region (indicated with a gray filled circle in Fig. 1). Though no special effort
152 was made to ensure a complete data record for the non-PSS, the majority of these sites
153 averaged better than 1 sonde/day.

154 Table 3 summarizes the number of sondes collected for each type of site. In total,
155 25,806 upper-air sondes were collected, quality controlled and are archived at the

156 DYNAMO data archive at NCAR/EOL (Earth Observing Lab). Included in this number
157 are ~5000 pilot balloons (pibals), which are winds only, generally in the lowest few km
158 of the troposphere. A map of the pibal sites is shown in Fig. 3. The red dots for the
159 Australian sites in this figure indicate that wind observations taken at these stations were
160 over a much greater vertical extent (e.g., up to 100 hPa). Typically, pibal observations in
161 the DYNAMO domain were taken at 06 and 18 UTC between rawinsonde observations at
162 00 and 12 UTC. Of the total soundings, 12,942 (~50%) are at hi-res. In comparison, the
163 TOGA-COARE data archive consists of 14,310 sondes of which 11,245 were at hi-res.

164 *b) Network performance*

165 Developing a research quality dataset begins with our ability to collect high-quality
166 data. Towards this end, a detailed list of “best sonde” launch practices (see sidebar on
167 sonde data quality assurance in Ciesielski et al. 2012) was established prior to the
168 experiment to guide station set-up and sonde operators. To our knowledge, these
169 guidelines were generally followed at the core sonde sites, which contributed to their
170 overall excellent performance and quality as will be shown. The launch success rate
171 (defined as the ratio of successful launches to those planned) for the 11 enhanced sites is
172 shown in Table 4. Values less than 100% are due to aborted or missed launches for a
173 variety of reasons generally related to weather or instrument issues. Ground system
174 equipment failures during parts of the EOP caused the lower rates at Nairobi
175 (11/24/2011-12/06/11) and Seychelles (10/01/11-10/27/11). The statistics for Gan in this
176 table are valid through 02/08/2012 when DOE intensive observations (8/day sondes)
177 ended prematurely due to political unrest in the Maldives. The overall success rate for the
178 six core sites during the SOP is ~98%.

179 One measure of a successful launch is the vertical extent of the observations (that is
180 to say, the higher the better). Table 4 lists the mean sonde termination (or burst) altitude
181 for the 11 enhanced sonde sites¹. Except for the *R/V Sagar Kanya*, this level is at or
182 above 75 hPa (~18 km) for all sites. These means are decreased slightly at some sites by
183 inclusion of a small number of sondes (listed in Table 4) that terminated at or below the
184 freezing level (~550 hPa) likely due to icing on the balloon.

185 Based on the number of sondes taken in DYNAMO along with their excellent
186 coverage in time and height, sonde operations were deemed an extraordinary success,
187 especially considering the remote location of many of the sites. Discussion in subsequent
188 sections will focus on the quality of the sonde data.

189 *c. Other data sources*

190 With the objective of providing reference observations for climate studies, the Global
191 Climate Observing System (GCOS) program is establishing a GCOS Reference Upper
192 Air Network (GRUAN, Immler and Sommer 2011) presently consisting of 15 sites with
193 an ultimate goal of 30-40 sites worldwide (Seidel et al. 2009). To assist in evaluating the
194 quality of the DYNAMO observation, GRUAN Vaisala RS92 (VRS92) data processing
195 was performed on data for three sites (Gan, Manus and Nauru). An advantage of the
196 GRUAN processed data is that it provides a comprehensive uncertainty analysis for each
197 observation (Immler et al. 2010).

198 To evaluate sonde humidity measurements, independent estimates of PW based on
199 GPS and MicroWave Radiometer (MWR) data were used. Eleven sonde sites (indicated

¹ The level at which a balloon bursts is a primarily function of balloon size, amount of gas used to fill balloon and weather conditions. These factors varied from site to site.

200 with red station names in Fig.1) had collocated GPS data and four of these locations
201 (Gan, Manus, Darwin and Nauru), being ARM-equipped sites, had collocated MWR data.
202 The reported accuracy of GPS and MWR PW retrievals is \sim 1-2 mm (Liou et al. 2001,
203 Bock et al. 2007, Wang et al. 2007) making them an excellent source for identifying
204 sonde biases (e.g., Wang and Zhang 2008). Since MWR observations are not reliable
205 when liquid water is present on the radiometer window, rain-contaminated MWR
206 estimates were removed if their PW value exceeded the sonde PW by 1.5σ , where σ is the
207 sonde PW standard deviation. For comparisons with sonde PW, the two-channel MWR
208 channel radiometer data, available at 1-min resolution, were averaged into 1-h bins. For
209 compatibility with the sonde and MWR measurements, the GPS data, being at either 30
210 min or 2 hr resolution (Wang et al. 2007) depending on the site, were binned to 1-h
211 resolution.

212 Satellite estimates of PW were obtained from the Microwave Integrated Retrieval
213 System (MiRS) PW product for the period 1 October 2011 to 14 February 2012. This
214 operational NOAA product is available on an hourly basis at \sim 0.1° resolution over all
215 surfaces and in all weather conditions. Details of the MiRS retrieval algorithm, which
216 blends microwave PW estimates from several satellites, and some performance statistics
217 can be found in Kidder and Jones (2007) and Boukabara et al. (2010).

218 Quality-controlled sonde data were used to evaluate relative humidity analyses from
219 two numerical weather prediction (NWP) centers: European Centre for Medium-range
220 Weather Forecasts (ECMWF) and the National Center for Environmental Prediction
221 (NCEP). Operational data from ECMWF were at 0.25° horizontal resolution, 20 vertical
222 levels from the surface to 20 hPa, whereas data from the NCEP Global Forecast System

223 (GFS) system were at 1° horizontal resolution, 32 vertical levels from the surface to 20
224 hPa. Both analyses were available at six-hourly intervals for the period 1 October to 31
225 December 2011. During the field phase of the experiment a major effort was undertaken
226 to ensure the real-time transmission of the sonde data onto the GTS for dissemination to
227 the operational NWP centers. Preliminary estimates indicate that ~95% of the soundings
228 from the core sonde network were received at the centers (Jeff Whiting, personal
229 communication) to be used in their data assimilation schemes.

230 **3. Quality control (QC) procedures**

231 This section describes the general processing of the hi-res sonde data which follows
232 the schemes outlined in Loehrer et al. (1996) and Ciesielski et al. (2012). While no
233 corrections are applied to GTS-resolution data due to lack of information describing
234 sonde type and age, sonde ascent rate, etc., gross limit checks and visual inspection were
235 used to flag questionable GTS data.

236 The first step in processing hi-res sonde data sets was to convert the raw sounding
237 data (Level 0 or L0) from the various data formats created by the different data systems
238 into a single, easily utilized format which we refer to as Level 1 (L1) processing. In
239 DYNAMO the hi-res sonde data came from 6 different sonde types (see Table 2) and 12
240 unique data formats. All hi-res sondes (L1 through L3) contain the basic fields (pressure,
241 height, temperature, relative humidity and winds), as well as ancillary fields (e.g., sonde
242 ascent rate and geolocation information) as a function of time. Header lines in each
243 sounding include the exact time of the sonde launch and the sonde serial number, which
244 provides information on the manufacture date that can prove helpful in developing
245 corrections.

246 These efforts were followed by Level 2 (L2) processing in which the hi-res soundings
247 were passed through a series of automated QC algorithms (Loehrer et al. 1996) and visual
248 inspection to systematically detect suspicious data values. Because of the unique data
249 format produced by the two ISS systems, L2 processing of data from these sites used
250 NCAR's Atmospheric Sounding Processing Environment (ASPEN) software. Details of
251 ASPEN can be found at: <http://www.eol.ucar.edu/isf/facilities/software/aspen/aspen.html>

252 In Level 3 (L3) processing, errors and biases in the data were identified and
253 corrected, if possible. With recent improvements in radiosonde technology, in particular
254 GPS-derived winds and ground station software, biases in temperature, pressure, and
255 winds are generally quite small (Nash et al. 2011) and their measurements are of suitable
256 quality for both weather and climate research. However, as will be seen in the next
257 section, special care must be taken in analyzing sonde data obtained from ships, which
258 may contain errors in the boundary layer temperature and humidity fields due to
259 contamination from the ship structure (Yoneyama et al. 2002)². L3 processing resulted
260 in the final high-resolution datasets that have either the necessary corrections applied or it
261 was determined that no additional corrections were necessary or possible.

262 While sonde manufacturers are continually striving to improve the accuracy of
263 humidity sensors, water vapor retrieval continues to be the most problematic variable
264 measured by upper-air sondes (Miloshevich et al. 2009; Nash et al. 2011). Since one of
265 primary goals of the experiment was to investigate the moistening processes during the
266 initiation phase of the MJO, a special effort was made to minimize humidity errors.

² Of course, soundings from islands and atolls also have local effects that make the data at low levels unrepresentative of the surrounding ocean. Depending on the application, this situation must be considered when evaluating the sounding data.

267 While use of well-calibrated surface data can provide an indication of low-level sonde
268 biases, independent estimates of PW are valuable for determining total-column biases.
269 Independent estimates of PW can come from several sources, including: ground-based
270 MWR retrievals (Cady-Pereira et al. 2008), satellite-based MW retrievals over the oceans
271 (Wentz 1997), and ground-based GPS estimates over land and on ships (Wang et al.
272 2007). Ideally the independent measurements should be collocated with the sonde
273 location. The next section describes the errors identified in the hi-res DYNAMO sonde
274 dataset and the details of their corrections.

275 Finally, in Level 4 (L4) processing a more “user-friendly” version of the sonde
276 dataset was created with QC flags assigned to each variable providing a measure of the
277 data’s reliability. L4 processing was performed on sites with both GTS-res and hi-res
278 data, where L3 hi-res data were vertically interpolated to create values at uniform
279 pressure intervals. Suspicious data were identified through application of both objective
280 QC test as in Loehrer et al. (1996) and subjective adjustment of QC flags by visual
281 inspection (Ciesielski et al. 2012). While tedious, visual inspection was necessary to
282 ensure a research-quality dataset since subtle errors in sonde data (e.g., superadiabatic
283 layers near cloud top due to wet bulbing effects as seen in Fig. 4, layers of suspicious
284 wind shear, boundary layer abnormalities, etc.) are often difficult to identify with
285 objective procedures. By flagging suspect data values, the reliable data are easily
286 retrievable with the users deciding what level of quality is acceptable for their analyses.

287 This second pass of QC checks and visual inspection, beyond those in L2, ensured the
288 veracity of the L3 corrections and provided yet another filter for identifying suspicious
289 values. Note that the QC checks and visual inspection in L2 and L4 processing did not

290 change any data values, only data quality flags. Additional details on interpolating the
291 data to uniform pressure intervals, objective tests for assigning QC flags, definition of
292 QC flags and the visual editor used to expedite this processing, can be found at:
293 www.eol.ucar.edu/projects/sondeqc/.

294 A summary of the various sonde dataset categories is provided in Table 5. Datasets
295 are referenced by both a level number and version number within each level. For
296 example, L3.0 signifies Level 3 version 0 of that dataset. If additional corrections are
297 needed in the future, the version number will be incremented accordingly (e.g., L3.1). For
298 sites with hi-res data, both L3 and L4 datasets are available from the DYNAMO data
299 archive. L1 and L2 datasets are available upon request to EOL. All hi-res datasets are
300 available in EOL-Sounding Composite (ESC) format which is a simple to read ASCII
301 format. Level 4 datasets are also provided in a simple ASCII format.

302 **4. Identification of errors, their correction and impact**

303 *a) Humidity corrections*

304 Of the 15 sites in DYNAMO using VRS92 upsondes, four of the sites (Malé, Gan,
305 Manus and *Mirai*) were running Digicora 3.64 (D3.64) ground station software. This
306 software version, introduced by Vaisala in 2010, provides humidity corrections for the
307 daytime soundings which include a solar radiation dry bias (SRDB) correction, and a
308 time-lag correction for the slow response of the humidity sensor at cold temperatures. No
309 humidity corrections are applied at night. Because of the proprietary nature of the
310 Digicora software, information on the details of these corrections is not available. The
311 SRDB, being the largest of the corrections, was first quantified in a study by Vömel et al.
312 (2007) which found relative RH dry biases ~9% near the surface increasing to > 50%

313 near 100 hPa. Changes to the coating of the VRS92 humidity sensor in 2006 and 2008
314 (Vaislala 2011) have reduced, but not eliminated these biases.

315 To evaluate the moisture measurements from these systems, Fig. 5 shows a
316 comparison over the diurnal cycle for Gan between sonde PW and two independent
317 estimates: a GPS and an ARM-deployed MWR. High temporal resolution MWR and
318 GPS data were averaged into hourly bins. This analysis considers only times when all
319 three instruments had reliable PW estimates (e.g., sonde moisture data must be present
320 from the surface up to 200 hPa and rain-contaminated MWR estimates were removed).
321 Differences between the sonde and MWR PW are less than 0.5 mm at individual hours
322 and only 0.2 mm in the mean. Similar agreement between sonde and MWR PW was
323 found at Manus (not shown) which also had MWR and GPS estimates of PW. *This*
324 *excellent agreement gives us confidence that the humidity measurements provided by the*
325 *sites using VRS92 sondes with D3.64 software need no further humidity corrections.*
326 Though a slight (~0.5 mm) moist bias is seen in the nighttime sonde data relative to the
327 MWR, this difference is well within the uncertainty of the MWR and sonde sensors. On
328 the other hand, for reasons unclear at this time, the GPS PW values at both Gan and
329 Manus are consistently ~2 mm lower than the other estimates. Standard deviation
330 estimates of the GPS minus sonde PW difference (bottom panel of Fig. 5) show that the
331 GPS PW biases are indeed significant. Despite the dry bias in the GPS observations, it is
332 noteworthy that all three estimates of PW show a similar diurnal trend with nighttime
333 values ~1.5 mm higher than those in the daytime.
334 Eleven sites in DYNAMO used VRS92 sondes (see Table 2) that did not have
335 software that included a SRDB correction. For sondes from these non-D3.64 sites, we

336 used a recent correction scheme developed by Wang et al. (2013) referred to as the
337 NCAR Radiation Bias Correction (NRBC). Designed to correct the SRDB and being a
338 function of pressure, temperature, RH and solar elevation angle, this easy-to-use
339 algorithm is based on the more complicated GRUAN correction. As in the Digicora
340 V3.64 software, the GRUAN algorithm also includes a calibration and time-lag
341 correction, although the exact nature and implementation of these corrections is
342 undoubtedly different between algorithms. Figure 6 shows a comparison of the mean
343 vertical profiles of RH (right panel) for the various corrections of Gan daytime sondes.
344 Differences in RH below 700 hPa among the three corrections (left panel) are quite small
345 (less than 1% at any given level). Since ~80% of the moisture for PW comes from the
346 surface to 700 hPa layer, consequently mean PWs computed with the corrected data show
347 excellent agreement (ranging from 52.3 to 52.5 mm) and lend confidence for using the
348 NRBC in DYNAMO. Application of NRBC increases PW ~0.8 mm in the daytime
349 sondes. The difference between the GRUAN and NRBC corrections above the freezing
350 level (~550 hPa) results primarily from GRUAN's calibration correction (Rudd Dirksen,
351 personal communication), since its time lag correction is of consequence only above 200
352 hPa but even then generally changes the mean RH < 1%. Due to its proprietary nature
353 the causes of the larger D3.64 corrections, particularly between 500 and 700 hPa, are
354 unknown. Since the calibration and time-lag corrections are less robust (i.e., biases within
355 the measurement uncertainty, Vömel et al. 2007) and result in insignificant changes to
356 PW (\leq 0.2 mm), they are not applied to the non-D3.64 VRS92 sondes.
357 To determine the need for humidity corrections in Meisei, Graw and Modem sondes
358 used at several sites in DYNAMO (see Table 1), data from the 8th WMO sonde

359 intercomparison study held in Yangjiang, China, in July 2010, were used. In this study 11
360 operational and two reference sondes were examined in 72 intercomparison launches
361 conducted in a variety of weather conditions and through the course of the 24-hour day.
362 Because of the small biases found in VRS92 V3.64 sondes in DYNAMO and their
363 excellent agreement to the reference CFH sondes in the WMO study (Nash et al 2011),
364 the VRS92 sondes are used here as a reference. Figure 7 shows the comparison of RH
365 profiles for day and nighttime dual launches for 3 sonde types compared to the VRS92.
366 The biases in the Graw sondes were within the stated accuracy of the RH measurements
367 of the VRS92 and Graw sensors (~5%), thus no bias correction is needed for this sonde
368 type. On the other hand, the size of the biases in the Modem and Meisei sondes indicate
369 that application of a correction would be beneficial.

370 To correct the Modem sondes at Ranai, the cumulative distribution function (CDF)
371 matching method was used. This method attempts to match the statistics of the problem
372 sonde (in this case, Modem) to those of the reliable sonde (i.e., VRS92). Details of this
373 method and examples of its application can be found in Nuret et al (2008) and Ciesielski
374 et al. (2010). Since the sondes at Ranai were released near 07 and 19 LT time,
375 intercomparison sonde launches within 2 hours of these times we used. With these
376 criteria, eight dual Modem-Vaisala twilight sondes were used in constructing the
377 correction table shown in Fig. 8. This table shows that the MODEM sondes have a moist
378 bias throughout most of the troposphere. Only at colder temperatures (< -50°C) and drier
379 conditions (RH < 60%) do the Modem sondes exhibit a dry bias relative to the Vaisala
380 sondes. Figure 9 shows the magnitude of the correction on the mean RH and specific
381 humidity (q) profiles. As one might expect based on Fig. 8, the correction has a drying

382 effect between 950 and 200 hPa and moistening above this level. The peak drying in
383 terms of q occurs around 800 hPa being ~ 0.4 g/kg. The corrected mean profile closely
384 resembles those from nearby sites (e.g., see Singapore profile shown later in Fig. 19) with
385 upper-level RHs approaching 85%.

386 As seen in Table 2, the Singapore site switched from Vaisala to Graw sondes on 21
387 December 2011. While this switch did not result in notable humidity biases per se, a
388 change in the launch procedure³ at this time resulted in suspicious low-level
389 thermodynamic fields. In fact, questionable T and T_d data were observed at low-levels (up
390 to 40 s after launch or the lowest 15-20 hPa) in $\sim 90\%$ of the Graw sondes. Because the
391 corrupted data can readily be identified by large, unrealistic gradients in the low-level T
392 and T_d fields (Fig. 10), a simple procedure was developed to correct these data. A visual
393 sonde editor was used to identify questionable data values in the 5-hPa interpolated sonde
394 (L4) dataset. In most cases the surface data, which comes from an independent data
395 source, were of good quality. In this case, new data were generated by linearly
396 interpolating between the surface value and good-quality data immediately above the
397 questionable data. In the few cases where the surface values were suspicious, a one-sided
398 second-order derivative was computed using good low-level L4 data. This gradient was
399 then used to extrapolate corrected values down to the surface. These corrections were
400 made in both the L3 (native resolution) and L4 datasets. An example of an uncorrected
401 and corrected low-level T and T_d profile is shown in Fig. 10.

402 As shown in Fig. 7c, the Meisei RS06G sondes used at 13 sites in DYNAMO had
403 humidity biases relative to the reliable VRS92 sondes. The humidity corrections of the

³ Graw sondes were launched from inside a building that was not acclimated to outside ambient conditions.

404 Meisei sondes, carried out at JAMSTEC, included procedures for removing: (1) a
405 discontinuity in RH at 0°C level due to deficiencies in Meisei's software (Sugidachi and
406 Fujiwara 2013) and (2) sonde RH biases using a CDF matching method based on 33
407 intercomparison launches (21 daytime and 12 nighttime) of VRS92 and Meisei sondes
408 conducted on Mirai cruises during DYNAMO. A daytime correction table was applied to
409 sondes launched from the local sunrise to sunset times; a nighttime correction table was
410 used for other local hours. A comparison of uncorrected and corrected sondes at Colombo
411 shows the impact of the corrections (Fig. 11). In the mean, the correction acts to moisten
412 sondes slightly below 800 hPa and dry them in a deep layer above this level with more
413 mid-level drying in the nighttime sondes as suggested by Fig. 7c. Because of the vertical
414 structure of the correction at Colombo, its mean PW decreased 0.4 mm while CAPE and
415 CIN increased 266 and 19 J kg⁻¹, respectively.

416 While no intercomparison datasets were available to correct the older model Sippican
417 and VIZ sondes used at three West Pacific sites, Wang and Zhang (2008) showed that
418 Sippican sondes have little bias at higher PW values such as observed in this region. A
419 comparison of EOP-mean PW for the VIZ sondes at Guam reveals that the sonde PW is
420 1.6 mm higher than the GPS PW (Fig. 14, later). While this difference is within the
421 uncertainty of the instruments, the magnitude of the GPS dry bias relative to the sonde
422 data is similar to what is seen at other DYNAMO sites (e.g., see Gan comparison in Fig.
423 5).

424 *b) Baseline corrections*

425 The standard WMO practice is to use surface data from a well-calibrated instrument
426 collocated with the sonde launch site as the bottom point of the sounding. These sonde-

427 independent observations can prove useful for identifying low-level biases in the sonde
428 data as demonstrated in TOGA COARE data where Wang et al. (2002) found large
429 differences between surface and boundary layer q indicating a sonde dry bias. During the
430 field phase of the experiment, monitoring of the low-level moisture gradient⁴ was
431 conducted using GTS resolution data. In this manner, the low-level moisture gradient at
432 Manus was found to be suspiciously negative in the mean, that is, q increased with height
433 in the lowest levels. A negative gradient was not observed at any other sites in the
434 DYNAMO domain. This led to an extensive investigation of the Manus sonde and
435 surface data in which Long and Holdridge (2012) determined that surface data from the
436 automated weather station (AWS) humidity sensor, which was being used to baseline the
437 Manus sounding, had an RH dry bias of about 5%. Furthermore, their report
438 recommended that the surface observations at Manus be switched to those from a nearby
439 surface meteorological (SMET) system that included a Vaisala HMP45 combined T/RH
440 probe in a forced air enclosure.

441 Since the 1-min SMET values were available for the entire DYNAMO EOP, the AWS
442 surface T and RH values were replaced with those from the SMET system using the 1-
443 min values closest to the time of launch. Figure 12 shows the diurnal cycle of the q
444 difference (δq) between the surface and the boundary layer mean, computed with AWS
445 (top) and SMET data (bottom). Using SMET data the mean low-level δq is now positive
446 at all hours of the day. The small mean moisture gradients observed at night even using
447 SMET data are related to the frequent (81% of the time) formation of shallow-surface
448 temperature inversions.

⁴ The low-level moisture gradient was computed as q at the surface minus q at the first point above the surface. A negative gradient indicates q increases with height.

449 Issues with baseline errors were also observed at Malé and the *Revelle*. To resolve the
450 problems at Malé, AWS values, which exhibited a modest dry bias, were recalibrated
451 using a highly accurate Vaisala HMP155 temperature/humidity probe. These improved
452 surface values were then used to baseline the Malé sondes. At the *Revelle*, a mismatch in
453 the level of the surface observations (19m) and where the sonde were released (2m) led to
454 disparity between the surface and 2m-sonde values, which resulted in several unphysical-
455 looking near-surface thermodynamic profiles. Because of this and the frequent
456 contamination of low-level sonde data by deck heating/cooling effects, the SMET values
457 were replaced by sonde data interpolated to the height of the SMET instrument (19 m)
458 with sonde data below this level eliminated in the L3 product.

459 *c. Ship deck heating/cooling corrections*

460 As shown in Yoneyama et al. (2002), low-level thermodynamic fields from ship
461 soundings can be distorted under certain conditions by the deck heating and cooling
462 effects. The magnitude of the distortion is a function of ship size, wind speed, and time of
463 day with larger impacts occurring for larger ships, weaker winds and during daylight
464 hours. In their analyses of sondes launched on the R/V *Mirai* (length 128 m, 8700 tons),
465 affected data were determined to be restricted to the lowest 40 m of the sonde profile. To
466 remove contaminated data, a simple procedure was designed which linearly extrapolates
467 good data above 50 m down to the surface. This procedure, based on a comparison of
468 regular ship soundings to those taken from a small boat measuring unaffected up-wind
469 conditions (Yoneyama et al. 2002), was applied to soundings from the R/Vs *Mirai*,

470 *Baruna Jaya* and *Sagar Kanya* which exhibited contaminated data⁵. The distortion of
471 low-levels fields on the *R/V Revelle* was more vertically limited due to its smaller size
472 (83 m, 2200 tons) such that eliminating the data below 19 m, as described above, was
473 sufficient to remove these effects. Also, a small percentage of the *Revelle* sondes had
474 temperature and humidity spikes, generally 5-10 s into the flight, likely caused by the
475 sonde passing through the ship smoke plume. The spikes were removed by setting the
476 data values in the affected layers to missing. Additional details on these and other
477 corrections in the *R/V Revelle* sondes are available in Young et al. (2012).

478 *d. Slow ascent soundings*

479 A small percentage of the hi-res Vaisala soundings (~5%) were classified as slow-
480 ascent sondes (ascent rates < 3 ms⁻¹) which may contain problematic RH profiles
481 containing artificial dry spikes. To eliminate problems with sensor icing, VRS92 sondes
482 are equipped with dual-heated RH sensors that are alternately heated⁶ while the non-
483 heated sensor measures the ambient RH (Miloshevich et al. 2009). If the sensors are not
484 adequately ventilated due to slow ascent resulting from either under-filling of the balloon
485 or icing on the balloon, the temperature gradient surrounding the heated sensor will not
486 have sufficient time to dissipate, resulting in artificially low RH measurements. An
487 example of these artificial dry spikes in a slow ascent sonde from the *R/V Mirai* is shown
488 in Fig. 13.

489 To mitigate this problem, the processing of slow-ascent sondes at the two ISS sites
490 included application of a special filtering within ASPEN to minimize the “dry spikes”.

⁵ A similar study conducted from the *R/V Baruna Jaya* during DYNAMO confirmed the reasonableness of this procedure for application to DYNAMO ship soundings.

⁶ Cycle for heated humidity instrument consist of 40s of heating followed by a 20s cool-down period.

491 At other sites, L2 processing marked layers with rapid RH fluctuations as suspicious data.
492 This information was then used in the L4 processing such that sondes with these layers of
493 suspicious data and slow ascent rates were given special attention. In this manner, L4
494 visual inspection of these layers with rapid RH fluctuations marked the QC flags for the
495 low RH values as bad and the high RH values as good. For the enhanced sites using
496 VRS92 sondes, ~15% of the slow ascents sondes exhibited dry spikes or < 1% of all
497 sondes.

498 **5. Assessment of moisture products**

499 *a) Further evaluation of sonde humidity*

500 Having demonstrated the accuracy of the sonde humidity data at few key sites
501 through comparison with independent estimates, Fig. 14 extends this analysis with
502 similar comparisons for several sites in the larger DYNAMO domain which had
503 collocated, independent estimates of PW. The PW means shown in this figure include
504 only times during the EOP when estimates from all sources were available at a given site.
505 Rain-contaminated MWR estimates were eliminated from the comparison. To ensure the
506 sensors are sampling similar volumes of the atmosphere, Wang et al. (2007) recommend
507 sonde and GPS comparisons only when the GPS sensor is within 50 km of the sonde
508 launch site and their elevation difference is less than 100 m. To provide more accurate
509 comparisons at sites with elevation differences > 10m, sonde PW was computed starting
510 at the elevation of the GPS sensor. This affected three sites: Singapore, Jakarta and
511 Seychelles, which had sensor height differences of 44, 129 and 537 m, respectively, with
512 the GPS sensor being higher in all cases.

513 At the four ARM sites with MWR estimates of PW, the sonde minus MWR PW
514 differences ranged from -0.2 to +0.5 mm lending confidence in the reliability of these
515 estimates. At all sites the GPS PW exhibits a dry bias relative to the sonde ranging from
516 -0.1 to -2.7 mm. The small GPS dry bias at Seychelles (-0.1 mm) may be related to a less
517 reliable sonde PW adjustment at this site to account for a large sensor height difference
518 (537 m). The overall mean GPS minus sonde PW difference among these eleven sites is
519 -1.7 mm (or ~3.5%). While this difference is within the range of measurement
520 uncertainty⁷, the consistent negative GPS bias among the sites together with the excellent
521 agreement of the sonde and MWR estimates suggests that the GPS PW estimates are, in
522 fact, too low. GPS PW dry biases have been noted in previous studies (e.g., Rocken et al.
523 1993, Tregoning et al. 1998, Wang et al. 2007). While future studies using GPS PW
524 should be aware of its dry bias, understanding the reasons for it are beyond the scope of
525 this study.

526 To evaluate the impact of the humidity corrections on some basic convective
527 parameters, Table 6 lists mean values of PW, CAPE and CIN for the six core DYNAMO
528 sites. Here CAPE and CIN were calculated assuming pseudo-adiabatic ascent using mean
529 thermodynamic conditions in the lowest 50hPa. For comparison with another tropical
530 experiment in which humidity corrections were carried out, values for TOGA COARE
531 are also listed. As one can see, total moisture is higher in the COARE domain consistent
532 with the higher SSTs there which results in higher CAPE and lower CIN. The impact of
533 the humidity corrections is an order of magnitude smaller in DYNAMO than in COARE.
534 In DYNAMO, the corrections result in a PW increase of 0.3 mm (or 0.6%) and CAPE

⁷ Based on the GRUAN uncertainty analysis for moisture, the uncertainty of the mean PW was ~4.5% for the three DYNAMO sites with GRUAN processed data.

535 and CIN increases of 75 J kg^{-1} and 6 J kg^{-1} , respectively. In contrast, the PW increase from
536 corrections of COARE soundings is 3.0 mm (or 5.6%) with CAPE and CIN increases of
537 450 J kg^{-1} and 17 J kg^{-1} , respectively. Similar large impacts from corrections were
538 observed at many sites in Terrain-influenced Monsoon Rainfall Experiment (TiMREX)
539 (Ciesielski et al. 2010).

540 *b) Evaluation of satellite and model humidity.*

541 The high quality and accuracy of the sonde moisture data, as demonstrated above,
542 make them a useful tool for validating moisture analyses from other sources. Since
543 satellite retrievals of PW have become increasingly utilized in recent years and important
544 for research and forecast applications of the water cycle, we examine the microwave
545 based MiRS PW product whose high temporal and spatial resolution make it convenient
546 for comparison to sonde data. Figure 15 shows a comparison of contemporaneous sonde
547 and MiRS PW at several sites in the DYNAMO domain. For these comparisons the
548 $\sim 0.1^\circ$ -resolution, hourly MiRS data were averaged in a circle with a 0.5° radius centered
549 on the sounding site location. At the majority of the sites, the mean MiRS PW bias is <
550 1.0 mm. Sites with higher biases are generally coastal sites on larger landmasses where
551 PW gradients are large due to complex topographic features (see mean PW map in Fig.
552 16). At 12 of the 13 sites examined, MiRS exhibits a dry bias relative to the sonde data
553 with an overall mean bias of -1.8 mm. The magnitude of this bias is similar to that
554 reported in Boukabara et al. (2010) where a global multi-site operational sonde and MiRS
555 comparison was conducted; however their analysis showed the MiRS being moister than
556 the sonde. Since a large fraction of rawinsondes used globally are characterized by a dry
557 bias (Wang and Zhang 2008), the MiRS moist bias found in their study may be related, in

558 part, to their use of uncorrected sonde data. Sonde and MiRS PW standard deviations are
559 quite similar at most sites and temporal correlations range from 0.55 to 0.91. It also
560 worth noting that even at sites with small mean biases, comparisons over the diurnal
561 cycle show considerably more scatter (not shown) such that MiRS does not appear to be a
562 useful tool for studying details of the diurnal cycle at open-ocean sites like Gan which
563 exhibit a small diurnal variations in PW (see Fig. 5).

564 As seen in Fig. 16, the meridional width of the equatorial moist tongue varies
565 considerably over the DYNAMO domain with a general west to east increase. The
566 narrowness of the moist tongue over the IO may make equatorial sites in this region more
567 susceptible to the dry air intrusions than in the West Pacific (Yoneyama and Parsons,
568 1999). Time series of PW at the six core DYNAMO sites (Fig. 17) show a modulation
569 on the time scale of the MJO. Dry periods are more pronounced at off-equatorial sites
570 like Malé and Colombo. Also the variation of PW on the MJO time scale is more
571 pronounced for the NSA sites. This is consistent with the findings of Johnson and
572 Ciesielski (2013) who showed a strong modulation of precipitation over the northern
573 array whereas the southern array experienced more persistent, yet briefer periods of
574 rainfall mostly related to ITCZ convection.

575 Because of the wide use of operational and reanalysis products (e.g., in process
576 studies, initializing numerical simulations, construction of large-scale forcing datasets for
577 cloud-resolving models, etc.), establishing their validity is important. Preliminary
578 comparisons of ECMWF and GFS operational analyses (OA) to sonde data show
579 excellent agreement in the basic fields (Johnson and Ciesielski 2013). Here we consider a
580 more detailed look at OA humidity fields. Figures 18-19 compare mean RH profiles

581 based on sonde and OA data for two near-equatorial DYNAMO sites: Gan and
582 Singapore. A comparison was also performed at Manus (in the western Pacific warm
583 pool) but is not shown due to its similarity to the Gan analyses. Mean profiles were
584 constructed from times during the period 1 October to 31 December 2011 when both
585 sonde and OA products were available. At these sites and Manus, the mean OA PWs
586 (shown in parentheses in Figs. 18 and 19) are within 1 mm of the sonde corrected PWs.
587 Both sonde and OA products captured a significant increase in moisture between Gan,
588 which lies near the western edge of the warm pool, and Singapore which lies about 30°
589 farther east within the Maritime Continent. This moisture gradient from the IO to the
590 maritime continent is consistent with the fact that DYNAMO occurred during a La Nina
591 when positive SST anomalies were present over the maritime continent and the western
592 Pacific (Johnson and Ciesielski 2013).

593 The ECWMF RH profiles show better overall agreement with corrected sonde profiles
594 than those from the GFS. The GFS profiles have a notable dry bias relative to the sonde
595 data in the boundary layer and a moist bias near 750 hPa. These biases in the GFS are
596 suggestive of an overactive shallow cumulus parameterization scheme that removes too
597 much boundary layer moisture and deposits it above 800 hPa. On the other hand, both
598 OA products are too moist above 300 hPa which leads to an overestimate in the
599 frequency of saturated layers. The upper-level moist bias is more pronounced in the GFS
600 data with more than double the frequency of saturated layers at Gan and Manus than
601 observed in the corrected sonde data. At Singapore the frequency of upper-level
602 saturated layers is comparable between the corrected sondes and ECMWF analysis.
603 Model temperature biases at upper-levels at Gan (i.e., a cool bias of 1°C at 100 hPa and

604 warm bias of 0.5°C at 200 hPa relative to sonde data, not shown) likely reflect radiative
605 feedbacks related to the enhanced model moisture and cloudiness between 100 and 200
606 hPa (Ackerman et al 1988).

607 Comparison of sonde and OA PW at several DYNAMO sites (Fig. 20) shows
608 agreement within the uncertainty of the sonde instruments. To facilitate this comparison
609 the OA were linearly interpolated to the sounding locations. Except at Nairobi where the
610 models exhibit a moist bias of 3-7%, the OA PWs generally exhibit a small dry bias
611 relative to the corrected sonde data. Part of the reason for the model dry bias at some sites
612 could be attributed to assimilation of uncorrected sonde data in the models. For example,
613 at Diego Garcia, which shows the largest model dry bias, the nighttime PW ECMWF bias
614 is -1.8 mm whereas the daytime bias (based on uncorrected sondes) is -2.9 mm. On the
615 other hand, at Manus corrected sondes were available for assimilation in real time yet the
616 OA products still show a dry bias of 3-4% at this site. Finally, small standard deviations
617 of sonde and model PW differences and high correlations (> 0.9 except at Singapore),
618 suggest that the OA products have done an excellent job in capturing the temporal
619 variability of moisture during DYNAMO.

620 **Summary and concluding remarks**

621 In terms of performance, considering both quantity and quality of upper-air sonde
622 observations, operations in DYNAMO should be considered an extraordinary success.
623 The upper-air sounding network for DYNAMO, which covered the tropics from Eastern
624 Africa to the West Pacific, included 72 sounding sites and dropsonde data from 13
625 aircraft missions. In total 25,806 sondes were collected from this network during the
626 experiment's 6-month extended observing period (EOP). This number includes 12,942

628 high vertical resolution sondes from 33 sites. Six core sounding sites in the central Indian
629 Ocean formed two sounding quadrilaterals one north and one south of the equator. These
630 arrays were intact for the majority of the 1 October to 30 November 2011 period, during
631 which time two prominent MJOs passed through the sonde network. Sounding data from
632 these core sites, as well as the larger network, will provide key observations for testing
633 many of the DYNAMO hypotheses.

634 Rigorous post-field phase processing of the sonde data included several levels of
635 quality checks and a variety of corrections that address a number of issues (e.g., daytime
636 time dry bias, errors in baseline surface data, ship deck-heating effects, artificial dry
637 spikes in slow-ascent sondes). Because of the importance of having accurate moisture
638 analyses, a significant portion of the post processing activities was directed towards
639 improving the quality of the humidity observations. Five of the six core sites used
640 research-quality Vaisala RS92 sondes. Small humidity biases in these sondes were further
641 reduced by application of additional corrections. While corrections are possible only at
642 sites with hi-res data, sonde data from all sites were processed with QC checks and visual
643 inspection to assign QC-flags to each variable. Part of the challenge of correcting the hi-
644 res data is that 6 different sonde types were involved. Using a variety of techniques, hi-
645 res sonde data from 30 sites were corrected to the standard of reference sondes.
646 Evaluation of corrected sonde data using independent estimates of PW at several key
647 sites showed mean PW biases of 0.5 mm or less which is well within the uncertainty
648 limits of these sensors. Compared with previous experiments such as TOGA COARE,
649 the humidity corrections applied in DYNAMO produced only small changes in the
650 moisture field (e.g., mean PW for the six core sites increased ~0.3 mm).

651 During the field phase of the experiment a major effort was undertaken to ensure the
652 real-time transmission of the DYNAMO sonde data onto the GTS for dissemination to
653 the operational NWP centers, which led to a 95% assimilation success rate. A comparison
654 of moisture products using corrected sondes and operational analyses from ECMWF and
655 GFS models shows an overall good agreement with a slight model PW dry bias at most
656 locations. Notable differences occur at upper-levels where model moisture and clouds are
657 more abundant than the sounding data would indicate.

658 In addition to the corrections described herein, work in is progress to correct for
659 influences of the Sri Lanka island flow blocking and diurnal cycle on low-level fields in
660 the Colombo soundings.⁸ Unless corrected, the large spacing between sounding sites (see
661 Fig. 1) causes these island-scale effects to be aliased onto larger scales, adversely
662 impacting fields and budget analyses over the NSA. Other islands in the DYNAMO core
663 sounding domain (Malé, Gan and Diego Garcia) are quite small ($< 10 \text{ km}^2$) and have only
664 a slight, yet detectable, impact on sonde observations. Efforts are underway primarily
665 using dropsonde data to quantify the impact of these smaller islands.

666 All sonde data described herein including documentation describing the processing
667 performed at each site are available from the EOL DYNAMO data archive:
668 http://data.eol.ucar.edu/master_list/?project=DYNAMO.

669 *Acknowledgments*

670 The success of the sounding operations for DYNAMO is due to countless students,
671 staff and scientists from many agencies and universities in Japan, Taiwan, Maldives and
672 the USA. In particular, we want to thank the Maldivian Meteorological Service for their

⁸ A north-south mountain range lies ~100 km to the east of the Colombo sonde site with peak elevations over 2500 m.

673 unfailing help during field operations. We also acknowledge support from Pay-Liam Lin
674 of National Central University, and Ben Jong-Dao Jou and Po-Hsuing Lin of National
675 Taiwan University for their assistance with supporting equipment and student staffing at
676 Malé. Enhancement of sounding operations at Seychelles, Nairobi and Colombo were
677 made possible by local staff collaborations as well as financial assistance from the WMO
678 and JMA. We greatly appreciate the efforts of Jim Moore and his team at NCAR EOL for
679 their guidance and logistical support of sounding operations during the experiment. We
680 also thank Wayne Schubert and Rick Taft for several insightful discussions, Holger
681 Vömel and Ruud Dirksen for making available the GRUAN corrected Vaisala data, John
682 Forsythe and Stan Kidder for providing the MiRS PW data, and the WMO for allowing
683 us to use their 8th sonde intercomparison dataset. Finally, special appreciation is extended
684 to Chidong Zhang for his exceptional efforts in orchestrating and implementing
685 DYNAMO. This research has been supported by the National Science Foundation under
686 Grants AGS-1059899 and AGS-1138353. Dr. Long acknowledges support from the
687 Office of Science of the U.S. Department of Energy as part of the ARM and Atmospheric
688 Systems Research (ASR) Programs.

689

690

691

692

693

694

695

696

697

698

699

700

701

References

- 702
703
704 Ackerman. T. P., K.-N. Liou, F. P. J. Valero, and L. Pfister, 1988: Heating rates in
705 tropical anvils. *J. Atmos. Sci.*, **45**, 1606-1623.
706 Bock, O., M.-N. Bouin, A. Walpersdorf, J. P. Lafore, S. Janicot, F. Guichard, and A.
707 Agusti-Panareda, 2007: Comparison of ground-based GPS precipitable water
708 vapour to independent observations and NWP model reanalysis over Africa.
709 *Quart. J. Roy. Meteor. Soc.*, **133B**, 2011-2027, doi: 10.1002/qj.185.
710 Boukabara, S.-A., K. Garrett and W. Chen, 2010: Global coverage of total precipitable
711 water using a microwave variational algorithm. *IEEE Transactions on Geoscience*
712 and *Remote Sensing*, **48**, 3608-3621.
713 Cady-Pereira, K. E., M. W. Shephard, D. D. Turner, E. J. Mlawer, S. A. Clough, and T. J.
714 Wagner, 2008: Improved daytime column-integrated precipitable water vapor
715 from Vaisala radiosonde humidity sensors. *J. Atmos. Oceanic Technol.*, **25**, 873–
716 883.
717 Ciesielski, P. E., and Coauthors, 2010: Quality controlled upper-air sounding dataset for
718 TiMREX/SoWMEX: Development and corrections. *J. Atmos. Oceanic Technol.*,
719 **27**, 1802–1821.
720 Ciesielski, P. E., P. T. Haertel, R. H. Johnson, J. Wang, and S. M. Loehrer, 2012:
721 Developing high-quality field program datasets. *Bull. Amer. Meteor. Soc.*, **93**, 325–
722 336.
723 Immel, F. J., and M. Sommer, 2011: Brief description of the RS92 GRUAN data product
724 (RS92-GDP). GRUAN Tech. Document GRUAN-TD-4, 17 pp. [Available online
725 at <http://www.gruan.org>.]

- 726 Immler, F. J., J. Dykema, T. Gardiner, D. N. Whiteman, P. W. Thorne, and H. Vömel,
727 2010: A guide for upper-air reference measurements: Guidance for developing
728 GRUAN data products. *Atmos. Meas. Tech. Discuss.*, **3**, 1217–1231, doi:10.5194/
729 amt-3-1217-2010.
- 730 Kidder S. Q. and A. S. Jones, 2007: A blended satellite total precipitable water product
731 for operational forecasting. . *J. Atmos. Ocean. Techol.*, **24**, 74-81.
- 732 Kuettner, J. P., D. E. Parker, D. R. Rodenhuis, H. Hoeber, H. Kraus, and G. Philander,
733 1974: GATE final international scientific plans. *Bull. Amer. Meteor. Soc.*, **55**,
734 711-744.
- 735 Johnson, R. H. and P. E. Ciesielski, 2013: Structure and properties of Madden-Julian
736 Oscillations deduced from DYNAMO sounding arrays. *J. Atmos. Sci.*, To be
737 published.
- 738 Liou Y., Y. Teng, T.V. Hove, and J. C. Liljegren, 2001: Comparison of precipitable water
739 observations in the near Tropics by GPS, microwave radiometer and radiosondes.
740 *J. Appl. Meteor.*, **40**, 5-15.
- 741 Loehrer, S. M., T. A. Edmands, and J. A. Moore, 1996: TOGA COARE upper-air
742 sounding data archive: development and quality control procedures. *Bull. Amer.*
743 *Meteor. Soc.*, **77**, 2651-2671.
- 744 Long, C. N., and D. J. Holdridge, 2012: Investigations of possible low-level temperature
745 and moisture anomalies during the AMIE field campaign on Manus Island. U.S.
746 Department of Energy. DOE-SC/ARM-TR-119. Available at:
747 www.arm.gov/publications/tech_reports/doe-sc-arm-tr-119.pdf

- 748 Miloshevich, L. M., H. Vömel, D. N. Whitman, and T. Leblanc, 2009: Accuracy
749 assessment and correction of Vaisala RS92 radiosonde water vapor
750 measurements. *J. Geophys. Res.*, **114**, D11305, doi:10.1029/2008JD011565.
- 751 Nash, J., T. Oakley, H. Vömel, and W. Li, 2011: WMO intercomparisons of high quality
752 radiosonde systems. WMO Tech. Doc. WMO/TD-1580, Instruments and
753 Observing Methods Rep. 107, 238 pp. [Available online at
754 http://www.wmo.int/pages/prog/www/IMOP/publications/IOM-107_Yangjiang.pdf.]
- 755 Nuret, M., J.-P. Lafore, F. Guichard, J.-L. Redelsperger, O. Bock, A. Agusti-Panareda,
756 and J.-B. N'Gamini, 2008: Correction of humidity bias for Vaisala RS80-A
757 sondes during the AMMA 2006 observing period. *J. Atmos. Oceanic Technol.*,
758 **25**, 2152–2158.
- 759 Rocken, C., R. H. Ware, T. Van Hove, F. Solheim, C. Alber, and J. Johnson, 1993:
760 Sensing atmospheric water vapor with the Global Positioning System, *Geophys.
761 Res. Lett.*, **20**, 2631–2634.
- 762 Seidel, D. J., and Coauthors, 2009: Reference upper-air observations for climate:
763 Rationale, progress, and plans. *Bull. Amer. Meteor. Soc.*, **90**, 361–369.
- 764 Sugidachi, T., and M. Fujiwara, 2013: Correction of the stepwise change observed at 0C
765 in Meisei RS2-91, RS-01G, and RS-06G radiosonde relative humidity profiles. *J.
766 Meteor. Soc. Japan*, **91**, 323–336.
- 767 Tregoning, P., R. Boers, D. O'Brien, and M. Hendy, 1998: Accuracy of absolute
768 precipitable water vapor estimates from GPS observations. *J. Geophys. Res.*, **103**,
769 28,701–28,710.
- 770

- 771 Vaisala, cited 2011: Sounding data continuity. [Available online at
772 <http://www.vaisala.com/en/products/soundingsystemsand>
773 radiosondes/soundingdatacontinuity/Pages/default.aspx.]
- 774 Vömel, H., and Coauthors, 2007: Radiation dry bias of the VaisalaRS92 humidity sensor.
775 *J. Atmos. Oceanic Technol.*, **24**, 953–963.
- 776 Wang, J., H. L. Cole, D. J. Carlson, E. R. Miller, K. Beierle, A. Paukkunen, and T. K.
777 Laine, 2002: Corrections of humidity measurement errors from the Vaisala RS80
778 radiosonde - Application to TOGA COARE data. *J. Atmos. Oceanic Technol.*, **19**,
779 981–1002.
- 780 Wang, J., and L. Zhang, 2008: Systematic errors in global radio-sonde precipitable water
781 data from comparisons with ground- based GPS measurements. *J. Climate*, **21**,
782 2218–2238.
- 783 Wang, J., L. Zhang, A. Dai, T. Van Hove, and J. Van Baelen, 2007: A near-global, 2-
784 hourly data set of atmospheric precipitable water from ground-based GPS
785 measurements. *J. Geophys. Res.*, **112**, D11107, doi:10.1029/2006JD007529.
- 786 Wang, J., L. Zhang, A. Dai, F. Immler, M. Sommer, and H. Vömel, 2012: Radiation dry
787 bias correction of Vaisala RS92 humidity data and its impact on historical
788 radiosonde data. *J. Atmos. Ocean. Techol.*, **30**, 197-214.
- 789 Webster, P. J., and R. Lukas, 1992: TOGA COARE: The Coupled Ocean-Atmosphere
790 Response Experiment. *Bull. Amer. Meteor. Soc.*, **73**, 1377–1416.
- 791 Wentz, F. J., 1997: A well calibrated ocean algorithm for special sensor microwave
792 imager, *J. Geophys. Res.*, **102**, 8703–8718.
- 793 Wu, X., M. W. Moncrieff, and K. A. Emmanuel, 2000: Evaluation of large-scale forcing

- 794 during TOGA COARE for cloud-resolving models and single-column models. *J.*
795 *Atmos. Sci.*, **57**, 2977-2985.
- 796 Yamanaka M. D., and Coauthors, 2008: HARIMAU radar-profiling network over the
797 Indonesian maritime continent: A GEOSS early achievement for hydrological
798 cycle and disaster prevention. *J. Disaster Research*, **3**, 78-88.
- 799 Yanai, M., S. Esbensen, and J. H. Chu, 1973: Determination of bulk properties of tropical
800 cloud clusters for large-scale heat and moisture budgets. *J. Atmos. Sci.*, **30**, 611-
801 627.
- 802 Yoneyama, K., and D. B. Parsons, 1999: A proposed mechanism for the intrusion of dry
803 air into the tropical West Pacific region. *J. Atmos. Sci.*, **56**, 1524-1546.
- 804 Yoneyama, K., M. Hanyu, F. Yoshiura, S. Sueyoshi, and M. Katsumata, 2002:
805 Radiosonde observation from the ship in the tropical region. *JAMSTECR (Tech*
806 *Rep)*, **45**, 31-39. Available from
807 http://www.godac.jamstec.go.jp/catalog/data/doc_catalog/media/shiken45_04.pdf
- 808 Yoneyama, K., C. Zhang, and C. N. Long, 2013: Tracking pulses of the Madden-Julian
809 Oscillation. *Bull. Amer. Meteor. Soc.*, (in press).
- 810 Young, K., J. Wang, W. Brown and D. Lauritsen, 2012: DYNAMO 2011 quality
811 controlled R/V *Revelle* radiosonde data set. Available from
812 <http://data.eol.ucar.edu/datafile/nph-get/347.099/readme.DYNAMO-2011.GAUS-Revelle-3rdRelease.pdf>)
- 813
- 814
- 815
- 816
- 817
- 818

819

List of Tables

820

821 1. Dates for various observing period in DYNAMO.

822 2. DYNAMO site information for stations for which high vertical resolution sonde data

823 were collected. Enhanced sites are in bold. Native resolution refers to the vertical time

824 resolution of the data received at NCAR EOL.

825 3. Inventory of upper-air sonde data. Note that the 24 sites with pibal data at 06 and 18

826 UTC, generally had rawinsonde data at 00 and 12 UTC.

827 4. Additional information for enhanced sonde sites. Launch success rate is defined as

828 percent of successful launches to number planned. Premature termination means sonde

829 did not ascend above freezing level (~550 hPa). Statistics for Gan are only through 08

830 February 2012 when DOE operations ended at this site.

831 5. Dataset naming convention with brief description of processing performed in each

832 level.

833 6. Convective parameter (CAPE, CIN and PW) statistics for six core DYNAMO sites for

834 1 October to 31 December and four TOGA COARE Intensive Flux Array (IFA) sites

835 for its 4-month IOP: showing range of mean site values, multi-site mean, and impact

836 of humidity correction on the parameter.

837

838

839

840

841

842

843

844

845

List of Figures

- 846 **Figure 1.** Upper-air sonde network for DYNAMO where color coding of dots indicates
847 the type of site including typical launch frequency. Enhanced sounding sites are
848 labeled with station name while priority sounding sites (PSS) are labeled with
849 WMO number. Red labels indicate sites with collocated GPS and/or MWR data.
850 High resolution sonde data were collected at 11 enhanced sites and 21 PSS (black
851 filled dots).
- 852 **Figure 2.** Visual sonde inventory of upper-air data for 6 core sites based on Level 4 data
853 (i.e., 5-hPa interpolated). Each line of dots represents a successful sonde launch.
854 Larger missing data gaps at *Revelle* and *Mirai* are the result of ship port calls.
- 855 **Figure 3.** DYNAMO pibal network with number of pibal (wind-only) soundings
856 indicated next to site. Wind data from these soundings generally are available
857 only in the lowest few kilometers of the atmosphere. Red dots at Australian sites
858 indicate that winds at these sites extended through depth of troposphere.
- 859 **Figure 4.** Skew-T for Ranai at 11UTC on 24 September 2011 showing “wetbulbing
860 effect” near 850 hPa. This effect results when a sonde is not properly ventilated
861 such that wetting of the thermistor in the cloud layer results in excessive cooling
862 by evaporation or sublimation once the sonde exits the cloud.
- 863 **Figure 5.** (top) Diurnal cycle of PW (mm) at Gan covering the period from 1 October to
864 14 January 2012 for three independent estimate (sonde – green, MWR – black,
865 GPS – red). Number in parentheses represent the period mean. (bottom) Dirunal
866 cycle of PW difference: GPS - sonde (red), MWR - sonde (black). Vertical red
867 lines show standard deviation of GPS – sonde PW difference. Number along the
868 lines show standard deviation of GPS – sonde PW difference. Number along the
869 lines show standard deviation of GPS – sonde PW difference. Number along the

870 bottom of plot indicate the number of comparison observations. Yellow shading
871 denotes daylight hours.

872 Figure 6. Mean vertical profiles of RH (%) with respect to water at Gan for daytime
873 sondes during the 1 October to 31 December 2011 period: (left panel) uncorrected
874 RH (black), GRUAN corrected (blue), NRBC corrected (green), Digicora 3.64
875 corrected (red); (right panel) difference between corrected and uncorrected
876 profiles. Mean PWs are listed in parentheses.

877 Figure 7. Vertical profiles of mean RH difference (%) between Vaisala RS92 (VRS92)
878 and (a) Modem, (b) Graw and (c) Meisei sondes for day (red) and nighttime
879 (blue) launches based on data from the WMO 2010 intercomparison study. A
880 positive (negative) difference indicates a moist (dry) bias in the sonde relative to
881 the Vaisala sonde. Numbers in parentheses indicate number of intercomparison
882 sondes that went into computing mean differences.

883 Figure 8. RH bias correction (%, contour increment of 3%) for Modem sondes covering
884 the full range of temperatures created by matching the Modem and VRS92 CDFs
885 for 8 dual launches. Axes are temperature and RH as observed by Modem sondes.
886 Light dotted line represents saturation with respect to ice.

887 Figure 9. Magnitude of humidity corrections at Ranai. (left) Mean corrected (red) and
888 uncorrected RH with respect to ice for $T < 0^\circ\text{C}$ (black) profiles, (middle) RH
889 difference due to correction, (right) q difference due to correction.

890 Figure 10. Example of low-level uncorrected 5-hPa sonde data at Singapore at
891 23UTC 03 January 2012 plotted on a skew-T diagram where black curve is T

892 and green curve is T_d . Filled red circles indicate data values identified as bad
893 data. Red lines show linear interpolation using good data.

894 Figure 11 Magnitude of humidity corrections at Colombo. (left) Mean corrected (red) and
895 uncorrected RH with respect to ice for $T < 0^\circ\text{C}$ (black) profiles, (middle) RH
896 difference due to correction, (right) q difference due to correction.

897 Figure 12. Diurnal cycle of $\Delta q = q_{sfc} - q_{bl}$, where q_{sfc} is surface q and q_{bl} is the boundary
898 layer mean computed from hi-res Manus sonde data: (top) computed using AWS
899 surface data, (bottom) computed using SMET data. Circles show values at
900 individual time, red line shows the mean diurnal cycle. Overall means are listed at
901 top of plots. Gray shading indicate nighttime hours.

902 Figure 13. Skew-T plot from *R/V Mirai* for 06 UTC 30 October 2011 showing suspicious
903 T_d data in the layer from 650 to 500 hPa. The ascent rate of the sonde in this layer
904 was $\sim 2.5 \text{ ms}^{-1}$ which resulted in poor ventilation of the sonde humidity sensor and
905 artificial dry spikes in the moisture profile (see text for further explanation).

906 Figure 14. PW estimates for several sites in the DYNAMO domain, listed from west to
907 east, from sonde (black bar), GPS (red bar) and MWR (cyan bar). (Top) shows
908 mean for times when all estimates at a given site were available during EOP.
909 (Bottom) shows PW bias defined as independent PW estimate minus sonde
910 estimate. Numbers along top of panel indicate the number of comparisons that
911 went into means.

912 Figure 15 Comparison of sonde PW statistics to MiRS PW (sonde– black bars, MiRS –
913 red bars) for 13 DYNAMO sites listed from west to east for period 1 October to
914 31 December 2011. (from top to bottom) PW means, PW difference where

915 negative values imply a MiRS dry bias, PW standard deviations, temporal
916 correlation coefficient of sonde PW estimates to MiRS product.

917

918 Figure 16. Mean PW map based on MiRS analyses for period 1 October to 31 December
919 2011. Location of DYNAMO sounding sites examined in Fig. 15 are shown on
920 map. Color scale at bottom is in mm.

921 Figure 17. Daily averaged PW time series for 6 core sites and (bottom) TRMM 3B42
922 rainfall averaged over the NSA. Mean PW is shown by thin gray line and is listed
923 in parentheses.

924 Figure 18. (left) Comparison of sonde and model mean RH profiles at Gan for the period
925 1 October to 31 December 2011 computed with sondes from all hours of 24 hour
926 day for uncorrected sonde (black), D3.64 corrected sonde (red), ECMWF (blue)
927 and GFS (green) data where model data were interpolated to Gan location.
928 Numbers in parentheses represent period mean. (right) Frequency of saturated
929 layers (RH \geq 100%) in 50 hPa layers. Analysis based on RH computed with
930 respect to ice of for $T < 0^\circ$

931 Figure 19. As in Fig. 18, except at Singapore for period 1 October to 21 December. Here
932 VRS92 sonde humidity was corrected using NRBC algorithm.

933 Figure 20. Comparison of sonde PW statistics to OA PW (ECMWF – black bars, GFS –
934 red bars) for 13 DYNAMO sites listed from west to east for period 1 October to
935 31 December 2011. (top) Difference in PW means (model – sonde) where
936 negative values imply a model dry bias, (middle) standard deviation of PW

937 difference, (bottom) temporal correlation coefficient of sonde PW estimates to
938 OA products.

939
940
941
942
943
944
945
946
947
948
949
950
951
952
953
954
955
956
957
958
959
960
961
962
963
964
965
966
967
968
969
970
971
972
973
974
975
976
977
978
979
980

981
982
983

Name	Dates	Comments
Special Observing Period (SOP)	10/01/11-11/30/11	SSA launched at 3-h frequency
Intensive Observing Period (IOP)	10/01/11-01/15/12	After SOP, Mirai offsite, Revelle and Diego at 6-h frequency
Extended Observing Period (EOP)	10/01/11-03/31/12	Gan to 1-2 sondes/day after 02/09.

984
985
986
987
988
989
990
991
992
993
994
995
996
997
998
999
1000
1001
1002
1003
1004
1005
1006
1007
1008
1009
1010
1011
1012
1013
1014
1015
1016
1017
1018

Table 1. Dates for various observing period in DYNAMO.

Site	Stn ID	Sonde type	vertical resolution	Number of sondes	Dates of retrieved data
Ambon	97724	Meisei RS06G	1 s	363	10/01/11 - 03/31/12
Baruna Jaya	YEAU	Vaisala RS92-SGP	2 s	58	12/05/11 - 12/18/11
Biak	97560	Meisei RS06G	1 s	347	10/01/11 - 03/31/12
Colombo	43466	Meisei RS06G	1 s	258	10/01/11 - 12/28/11
Darwin	94120	Vaisala RS92-15	2 s	397	10/01/11 - 03/31/12
Diego Garcia	DRG	Vaisala RS92-SGP	1 s	679	09/30/11 - 01/15/12
P3 dropsondes	NOAA3	Vaisala RS92-SGP	0.25 s	469	11/09/11 - 12/13/11
Gan	43599	Vaisala RS92-SGP	2 s	1118	09/23/11 - 03/31/12
Guam	91212	VIZ B2	6 s	297	10/01/11 - 03/31/12
Jakarata	96749	Meisei RS06G	1 s	356	10/01/11 - 03/31/12
Koror	91408	Sippican Mark IIA	1 s	339	10/01/11 - 03/31/12
Kupang	97372	Meisei RS06G	1 s	349	10/01/11 - 03/31/12
Makassar	97180	Meisei RS06G	1 s	337	10/01/11 - 03/31/12
Malé	43555	Vaisala RS92-SGP	2 s	323	09/29/11 - 12/15/11
Manado	97014	Meisei RS06G	1 s	361	10/01/11 - 03/31/12
Manus	92044	Vaisala RS92-SGP	2 s	1411	09/25/11 - 03/31/12
Medan	96035	Meisei RS06G	1 s	364	10/01/11 - 03/31/12
Merauke	97980	Meisei RS06G	1 s	364	10/01/11 - 03/31/12
Mirai	JNSR	Vaisala RS92-SGP	2 s	518	09/26/11 - 12/10/11
Nairobi	63741	Vaisala RS92-SGP	2 s	198	09/01/11 - 03/05/12
Nauru	91532	Vaisala RS92-SGP	2 s	337	10/01/11 - 03/30/12
Padang	96163	Meisei RS06G	1 s	421	10/01/11 - 03/31/12
Palu	97072	Meisei RS06G	1 s	365	10/01/11 - 03/31/12
Pangkal	96237	Meisei RS06G	1 s	297	10/05/11 - 03/31/12
Pontianak	96851	Vaisala RS92-SGP	2 s	57	12/03/11 - 01/01/12
Ranai	96147	Modem M2K2DC	1 s	321	09/08/11 - 02/29/12
Revelle	KAOU	Vaisala RS92-SGP	1 s	635	08/30/11 - 02/10/12
Sagar Kanya	VTJR	Vaisala RS92-SGP	2 s	71	09/25/11 - 10/19/11
Seychelles	63985	Vaisala RS92-SGP	2 s	320	10/28/11 - 03/31/12
Singapore	48698	Vaisala RS92-SGP Graw DMF-09	2 s 1 s	163 202	10/01/11 - 12/21/11 12/21/11 - 03/31/12
Sipora		Vaisala RS92-SGP	2 s	215	11/29/11 - 01/01/12
Surabaya	96935	Meisei RS06G	1 s	365	10/01/11 - 03/31/12
Yap	91413	Sippican Mark IIA	1 s	267	09/30/11 - 03/31/12

1019

1020

1021 Table 2. DYNAMO site information for stations for which high vertical resolution sonde
1022 data were collected. Enhanced sites are in bold. Native resolution refers to the vertical
1023 time resolution of the data received at NCAR EOL.

1024

1025

1026

1027

1028

1029

1030

1031

1032

1033

1034
1035
1036
1037

Site type	Number of sites	Vertical resolution	Number of sondes
Enhanced	11	1-2 s	5589
P3-dropsondes	1	0.25 s	469
PSS (hi-res)	21	1-6 s	6884
PSS (low-res)	24	15-25 hPa	5078
Non PSS (low-res)	16	15-25 hPa	2581
Pibal (winds only)	27	30-40 hPa	5205
Total	73		25806

1038
1039
1040
1041
1042
1043
1044
1045
1046
1047
1048
1049
1050

Site	Number of Sondes	Launch Success Rate (%)	Missed launches	Mean burst altitude (hPa)	Number of premature terminations
<i>Baruna Jaya</i>	58	100.0	0	41.2	0
Colombo	258	93.8	17	66.2	0
Diego Garcia	679	98.4	11	69.9	13
Gan	1066	97.8	24	60.5	24
Malé	323	100.0	0	53.8	0
Manus	1411	93.4	99	62.8	46
<i>Mirai</i>	518	100.0	0	43.0	3
Nairobi	198	71.6	78	32.4	3
<i>Revelle</i>	635	98.4	10	72.9	13
<i>Sagar Kanya</i>	71	97.3	2	136.0	0
Seychelles	320	85.8	53	33.2	2

1051
1052
1053
1054
1055
1056
1057
1058
1059

Table 4. Additional information for enhanced sonde sites. Launch success rate is defined as percent of successful launches to number planned. Premature termination means sonde did not ascend above freezing level (~550 hPa). Statistics for Gan are only through 08 February 2012 when DOE operations ended at this site.

1060
1061
1062
1063

Level	Description
Level 0 (L0)	Raw, unprocessed hi-res data in original formats
Level 1 (L1)	Initial hi-res data: uniform, easily readable format
Level 2 (L2)	Preliminary hi-res data: processed with automated and visual QC
Level 3 (L3)	Final hi-res data: corrected for biases and errors if necessary
Level 4 (L4)	Uniform vertical resolution data created from hi-res datasets and GTS-res sondes processed with objective QC checks and visual inspection.

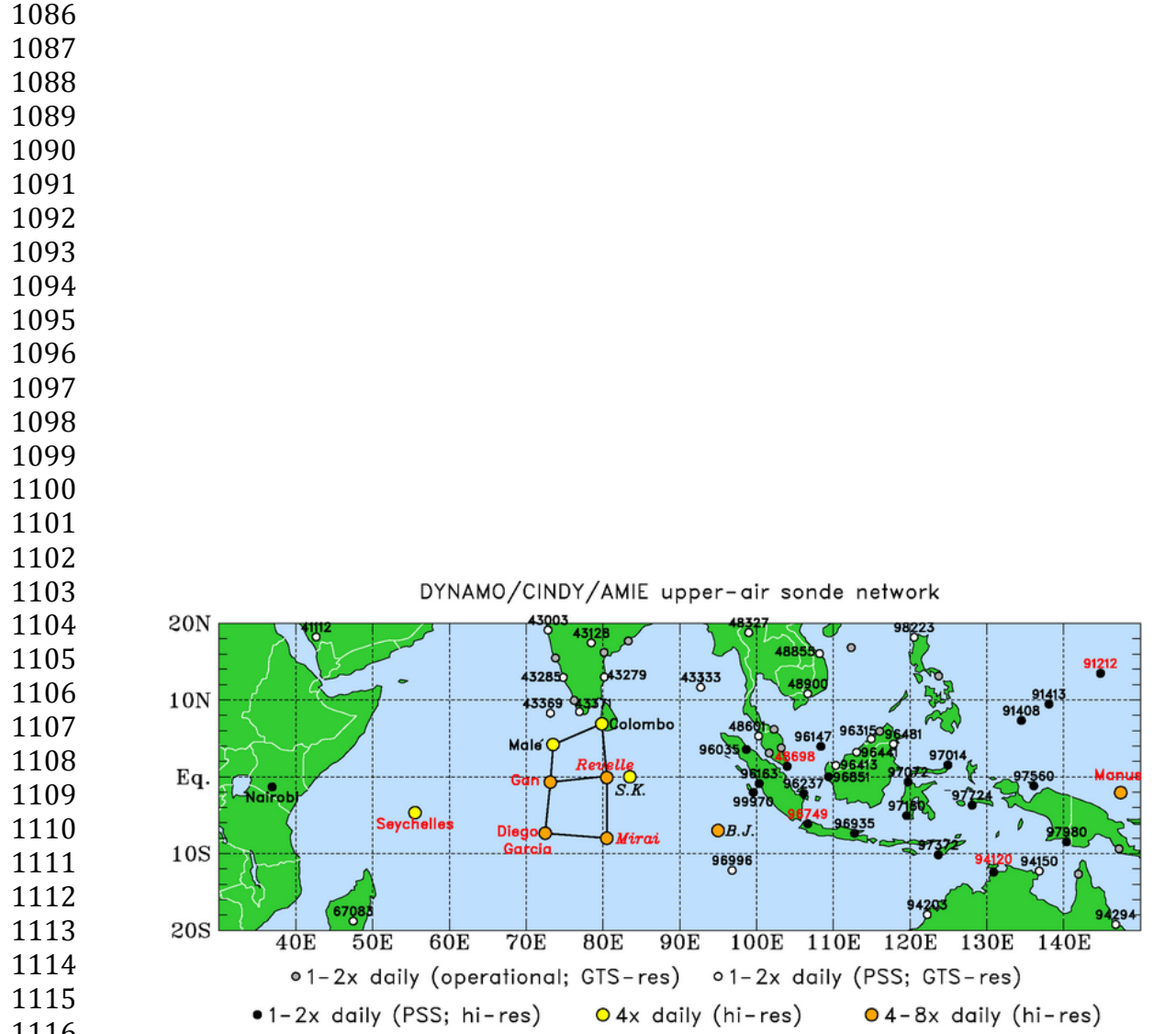
1064
1065
1066
1067
1068
1069
1070
1071
1072
1073

Table 5. Dataset naming convention with brief description of processing performed in each level.

	DYNAMO core sites	TOGA COARE IFA sites
PW (mm) range	46.4 to 55.1	52.0 to 55.1
PW (mm) mean	51.7	53.3
PW (mm) correction	+0.3	+3.0
CAPE (J kg^{-1}) range	846 to 1499	1235 to 1529
CAPE (J kg^{-1}) mean	1207	1529
CAPE (J kg^{-1}) correction	+75	+450
CIN (J kg^{-1}) range	-91 to -42	-43 to -28
CIN (J kg^{-1}) mean	-61	-34
CIN (J kg^{-1}) correction	+6	+17

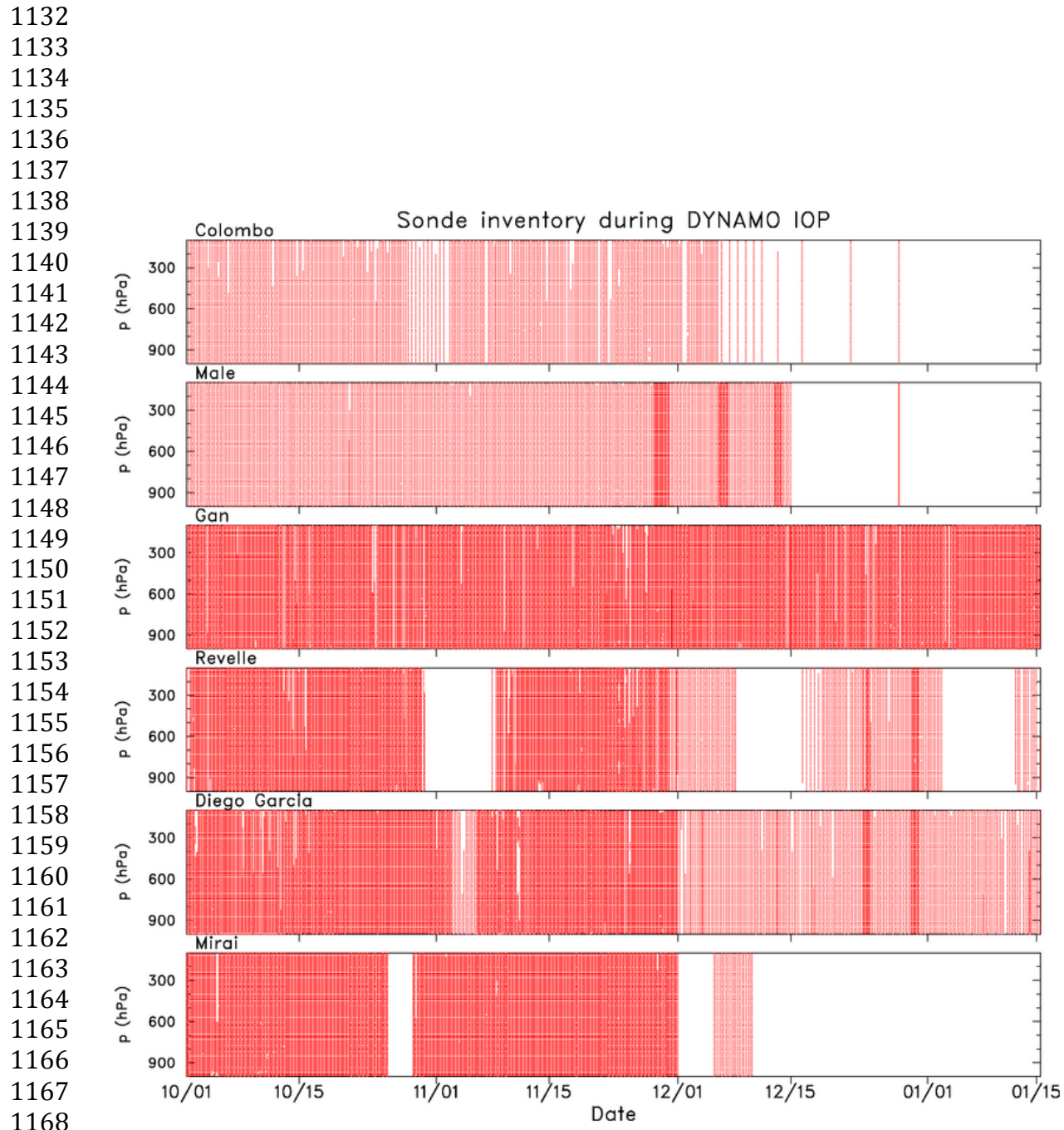
1074
1075
1076
1077
1078
1079
1080
1081
1082
1083
1084
1085

Table 6. Convective parameter (CAPE, CIN and PW) statistics for six core DYNAMO sites for 1 October to 31 December and four TOGA COARE Intensive Flux Array (IFA) sites for its 4-month IOP: showing range of mean site values, multi-site mean, and impact of humidity correction on the parameter.



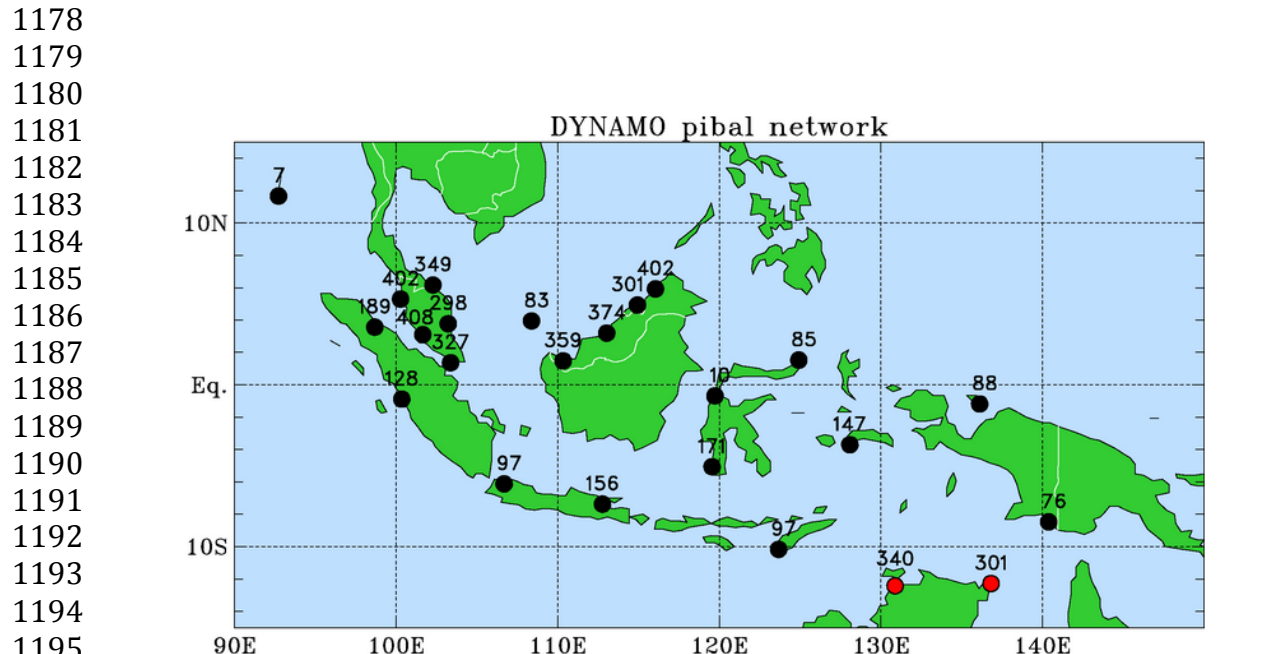
1114
1115
1116
1117
1118
1119 FIG. 1. Upper-air sonde network for DYNAMO where color coding of dots indicates
1120 the type of site including typical launch frequency. Enhanced sounding sites are
1121 labeled with station name while priority sounding sites (PSS) are labeled with WMO
1122 number. Red labels indicate sites with collocated GPS and/or MWR data. High
1123 resolution sonde data were collected at 11 enhanced sites and 21 PSS (black filled
1124 dots).

1125
1126
1127
1128
1129
1130
1131



1170 FIG. 2. Visual sonde inventory of upper-air data for 6 core sites based on Level 4 data
 1171 (i.e., 5-hPa interpolated). Each line of dots represents a successful sonde launch.
 1172 Larger missing data gaps at *Revelle* and *Mirai* are the result of ship port calls.

1173
 1174
 1175
 1176
 1177



1197 FIG. 3. DYNAMO pibal network with number of pibal (wind-only) soundings
 1198 indicated next to site. Wind data from these soundings generally are available only in
 1199 the lowest few kilometers of the atmosphere. Red dots at Australian sites indicate that
 1200 winds at these sites extended through depth of troposphere.

1201
 1202
 1203
 1204
 1205
 1206
 1207
 1208
 1209
 1210
 1211
 1212
 1213
 1214
 1215
 1216
 1217
 1218
 1219
 1220
 1221
 1222
 1223

1224
1225
1226
1227
1228
1229
1230
1231
1232
1233
1234
1235
1236
1237
1238
1239
1240
1241
1242
1243
1244
1245
1246
1247
1248
1249
1250
1251
1252
1253
1254
1255
1256
1257
1258
1259
1260
1261
1262
1263
1264
1265
1266
1267
1268
1269

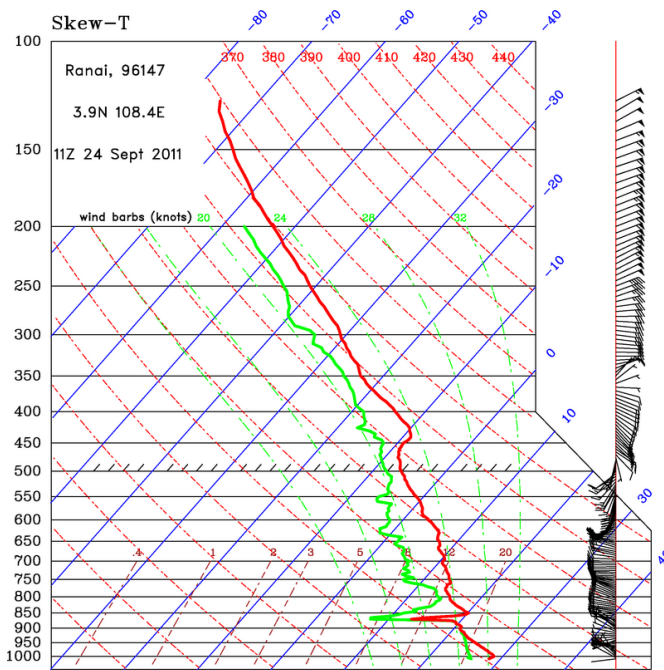


FIG. 4. Skew-T for Ranai at 11UTC on 24 September 2011 showing “wetbulbing effect” near 850 hPa. This effect results when a sonde is not properly ventilated such that wetting of the thermistor in the cloud layer results in excessive cooling by evaporation or sublimation once the sonde exits the cloud.

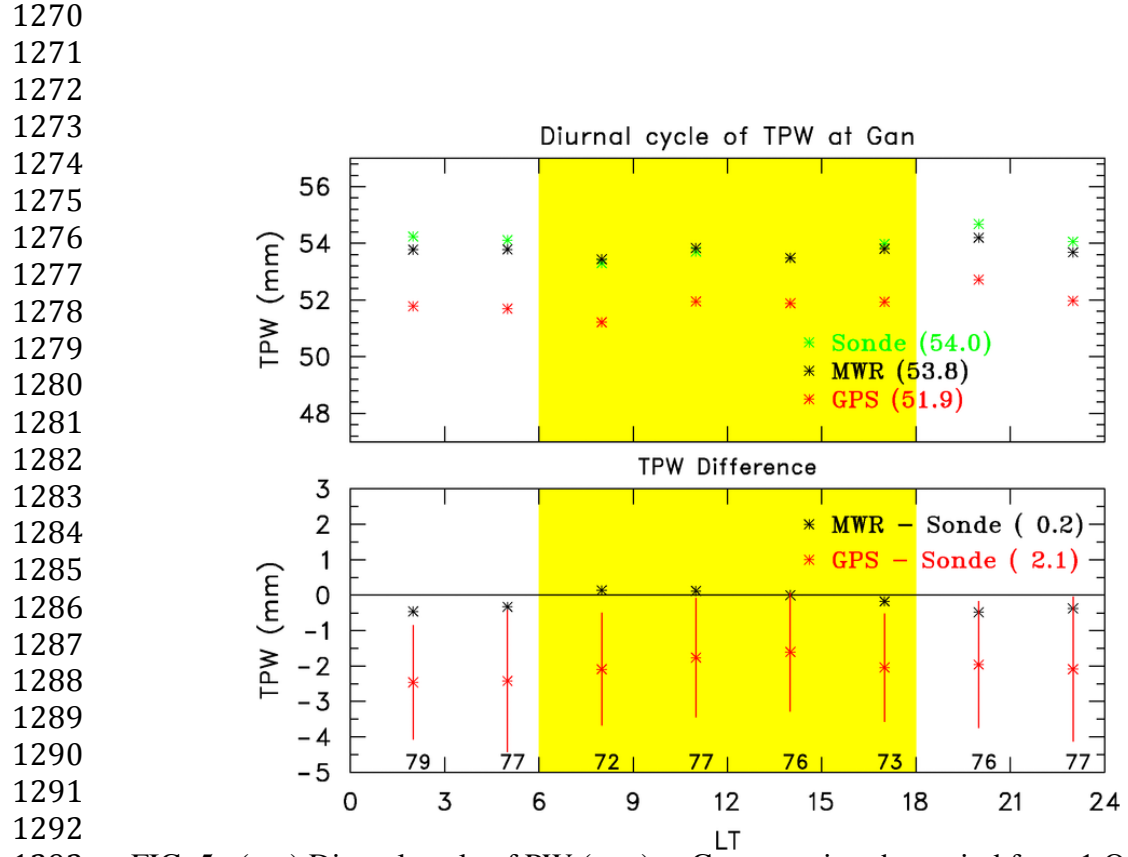
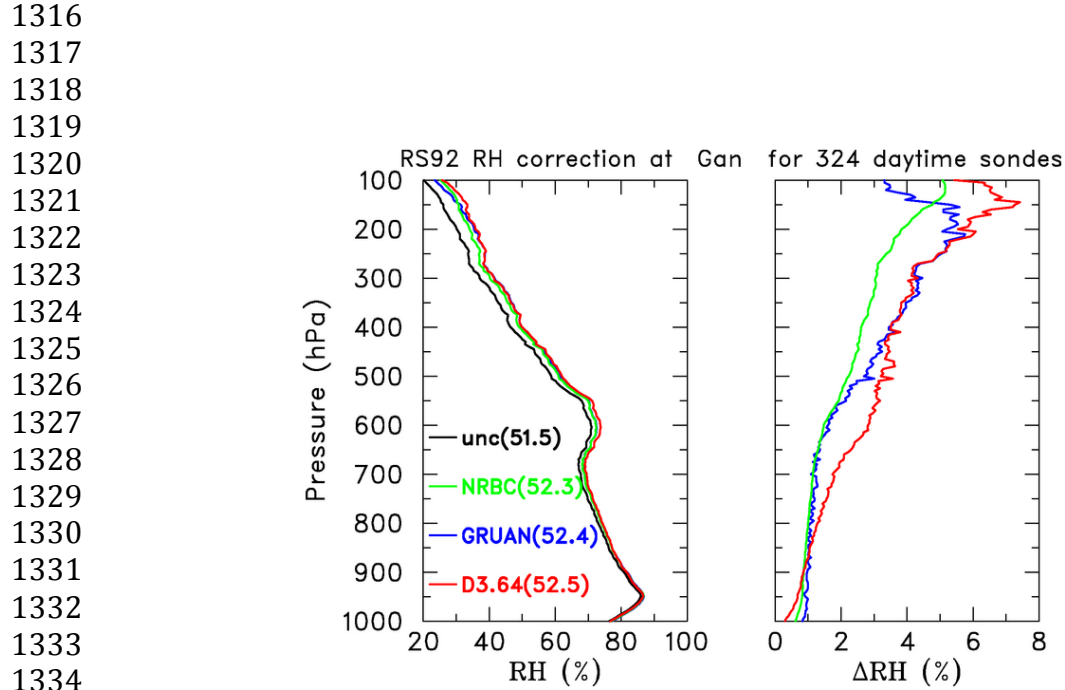


FIG. 5. (top) Diurnal cycle of PW (mm) at Gan covering the period from 1 October to 14 January 2012 for three independent estimate (sonde – green, MWR – black, GPS – red). Number in parentheses represent the period mean. (bottom) Diurnal cycle of PW difference: GPS - sonde (red), MWR - sonde (black). Vertical red lines show standard deviation of GPS – sonde PW difference. Number along the bottom of plot indicate the number of comparison observations. Yellow shading denotes daylight hours.



1335 FIG. 6. Mean vertical profiles of RH (%) with respect to water at Gan for daytime sondes
 1336 during the 1 October to 31 December 2011 period: (left panel) uncorrected RH (black),
 1337 GRUAN corrected (blue), NRBC corrected (green), Digicora 3.64 corrected (red); (right
 1338 panel) difference between corrected and uncorrected profiles. Mean PWs are listed in
 1339 parentheses.

1340
 1341
 1342
 1343
 1344
 1345
 1346
 1347
 1348
 1349
 1350
 1351
 1352
 1353
 1354
 1355
 1356
 1357
 1358
 1359
 1360
 1361

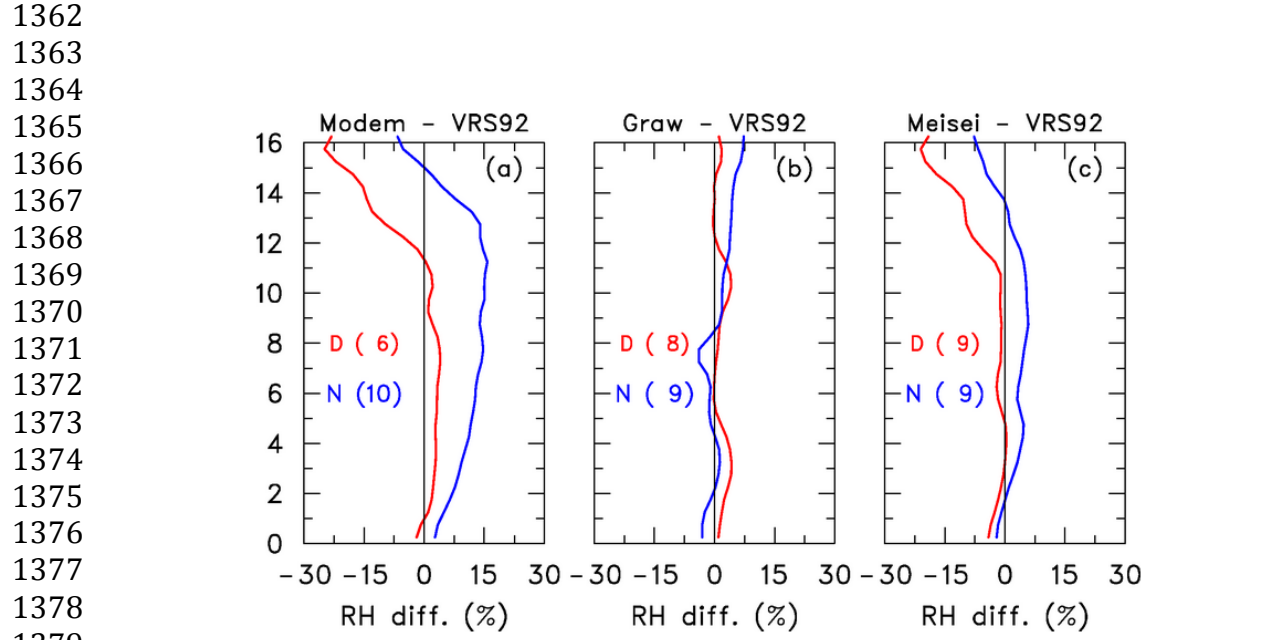
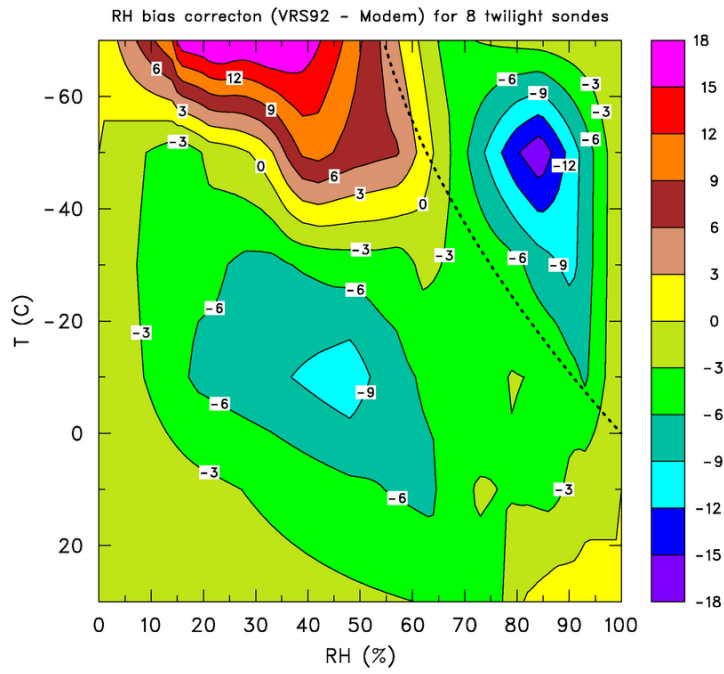


FIG. 7. Vertical profiles of mean RH difference (%) between Vaisala RS92 (VRS92) and (a) Modem, (b) Graw and (c) Meisei sondes for day (red) and nighttime (blue) launches based on data from the WMO 2010 intercomparison study. A positive (negative) difference indicates a moist (dry) bias in the sonde relative to the Vaisala sonde. Numbers in parentheses indicate number of intercomparison sondes that went into computing mean differences.

1408
1409
1410
1411
1412
1413
1414
1415
1416
1417
1418
1419
1420
1421
1422
1423
1424
1425
1426
1427
1428



1429 FIG. 8. RH bias correction (%, contour increment of 3%) for Modem sondes covering the
1430 full range of temperatures created by matching the Modem and VRS92 CDFs for 8 dual
1431 launches. Axes are temperaure and RH as observed by Modem sondes. Light dotted line
1432 represents saturation with respect to ice.

1433
1434
1435
1436
1437
1438
1439
1440
1441
1442
1443
1444
1445
1446
1447
1448
1449
1450
1451
1452
1453

1454
1455
1456
1457
1458
1459
1460
1461
1462
1463
1464
1465
1466
1467
1468
1469
1470
1471
1472
1473
1474
1475
1476
1477
1478
1479
1480
1481
1482
1483
1484
1485
1486
1487
1488
1489
1490
1491
1492
1493
1494
1495
1496
1497
1498
1499

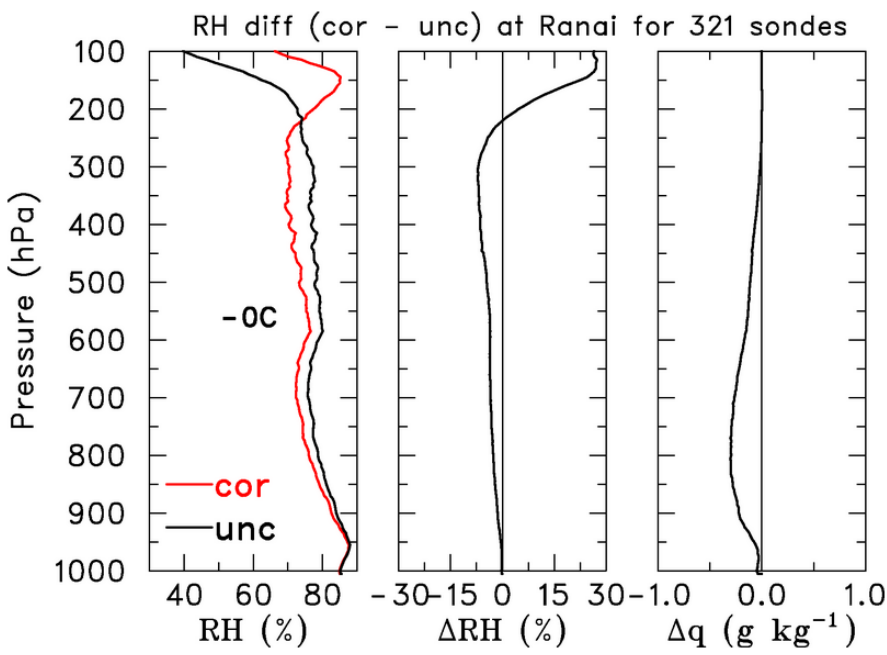


FIG. 9. Magnitude of humidity corrections at Ranai. (left) Mean corrected (red) and uncorrected RH with respect to ice for $T < 0^\circ\text{C}$ (black) profiles, (middle) RH difference due to correction, (right) q difference due to correction.

1500
1501
1502
1503
1504
1505
1506
1507
1508
1509
1510
1511
1512
1513
1514
1515
1516
1517
1518
1519
1520
1521
1522

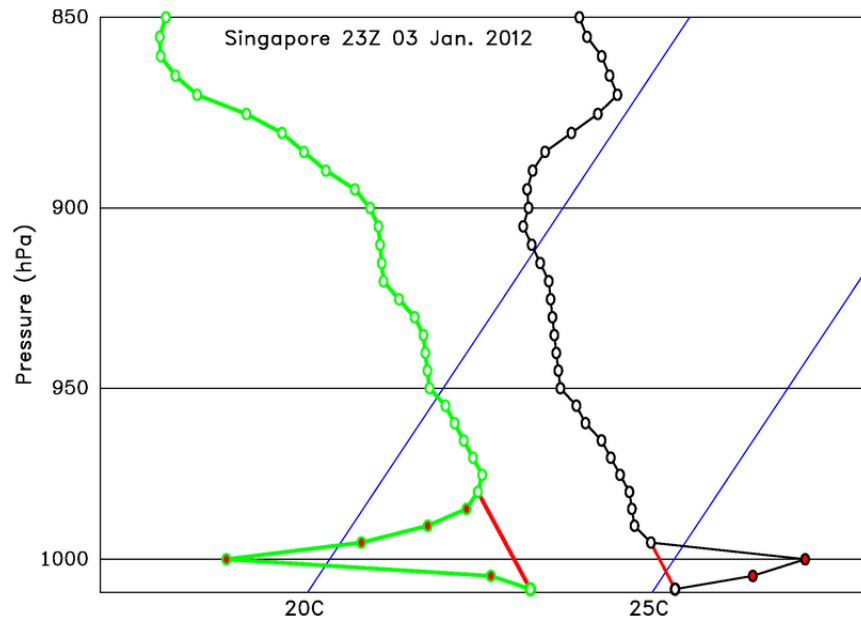
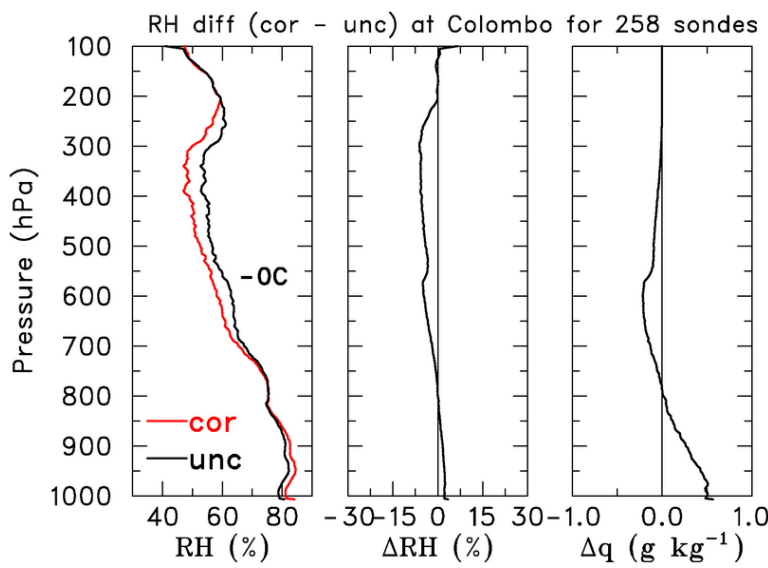


FIG. 10. Example of low-level uncorrected 5-hPa sonde data at Singapore at 23UTC 03 January 2012 plotted on a skew-T diagram where black curve is T and green curve is T_d . Filled red circles indicate data values identified as bad data. Red lines show linear interpolation using good data.

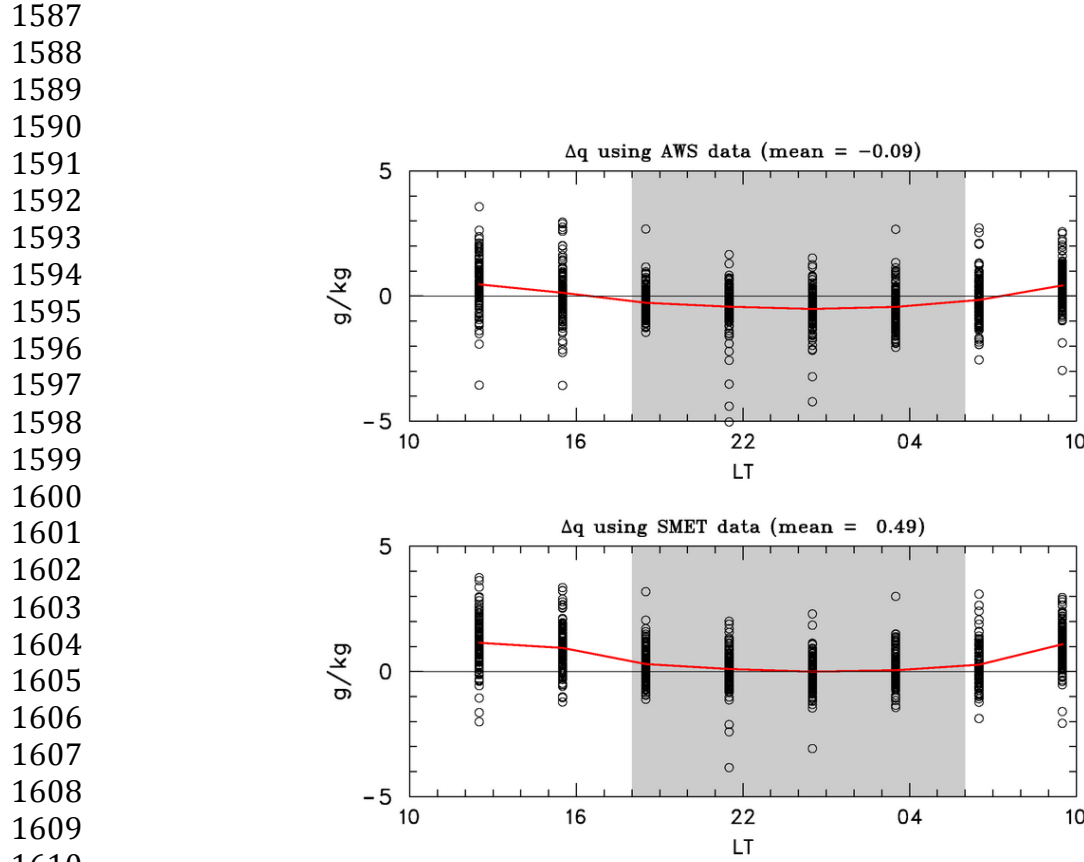
1523
1524
1525
1526
1527
1528
1529
1530
1531
1532
1533
1534
1535
1536
1537
1538
1539
1540

1541
1542
1543
1544
1545
1546
1547
1548
1549
1550
1551
1552
1553
1554
1555
1556
1557



1558 FIG. 11 Magnitude of humidity corrections at Colombo. (left) Mean corrected (red) and
1559 uncorrected RH with respect to ice for $T < 0^\circ\text{C}$ (black) profiles, (middle) RH difference
1560 due to correction, (right) q difference due to correction.

1561
1562
1563
1564
1565
1566
1567
1568
1569
1570
1571
1572
1573
1574
1575
1576
1577
1578
1579
1580
1581
1582
1583
1584
1585
1586



1611 FIG. 12. Diurnal cycle of $\Delta q = q_{sfc} - q_{bl}$, where q_{sfc} is surface q and q_{bl} is the boundary
 1612 layer mean computed from hi-res Manus sonde data: (top) computed using AWS
 1613 surface data, (bottom) computed using SMET data. Circles show values at individual
 1614 time, red line shows the mean diurnal cycle. Overall means are listed at top of plots.
 1615 Gray shading indicate nighttime hours.

1616
 1617
 1618
 1619
 1620
 1621
 1622
 1623
 1624
 1625
 1626
 1627
 1628
 1629
 1630
 1631
 1632

1633
1634
1635
1636
1637
1638
1639
1640
1641
1642
1643
1644
1645
1646
1647
1648
1649
1650
1651
1652
1653
1654
1655
1656
1657
1658
1659
1660
1661
1662
1663
1664
1665
1666
1667
1668
1669
1670
1671
1672
1673
1674
1675
1676
1677
1678

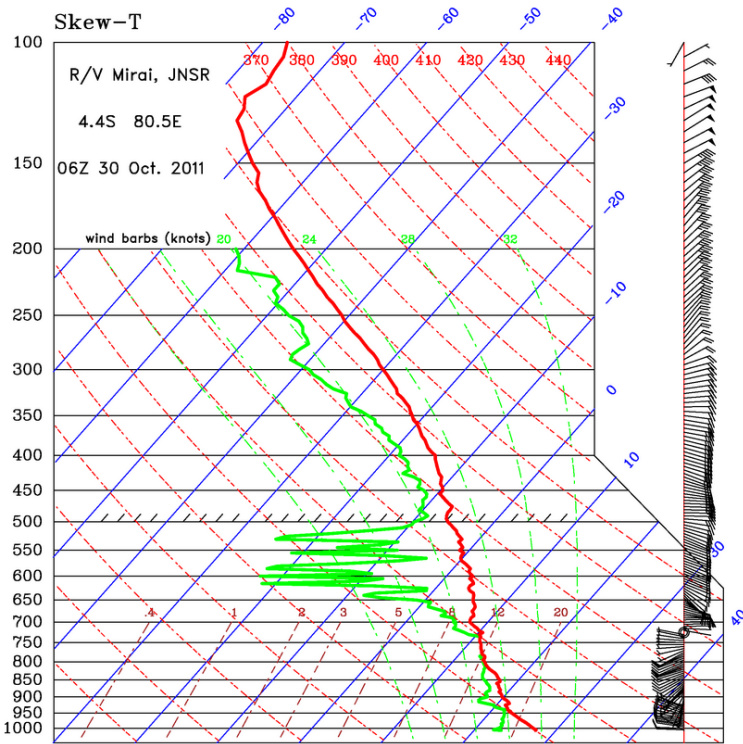


FIG. 13. Skew-T plot from *R/V Mirai* for 06 UTC 30 October 2011 showing suspicious T_d data in the layer from 650 to 500 hPa. The ascent rate of the sonde in this layer was $\sim 2.5 \text{ ms}^{-1}$ which resulted in poor ventilation of the sonde humidity sensor and artificial dry spikes in the moisture profile (see text for further explanation).

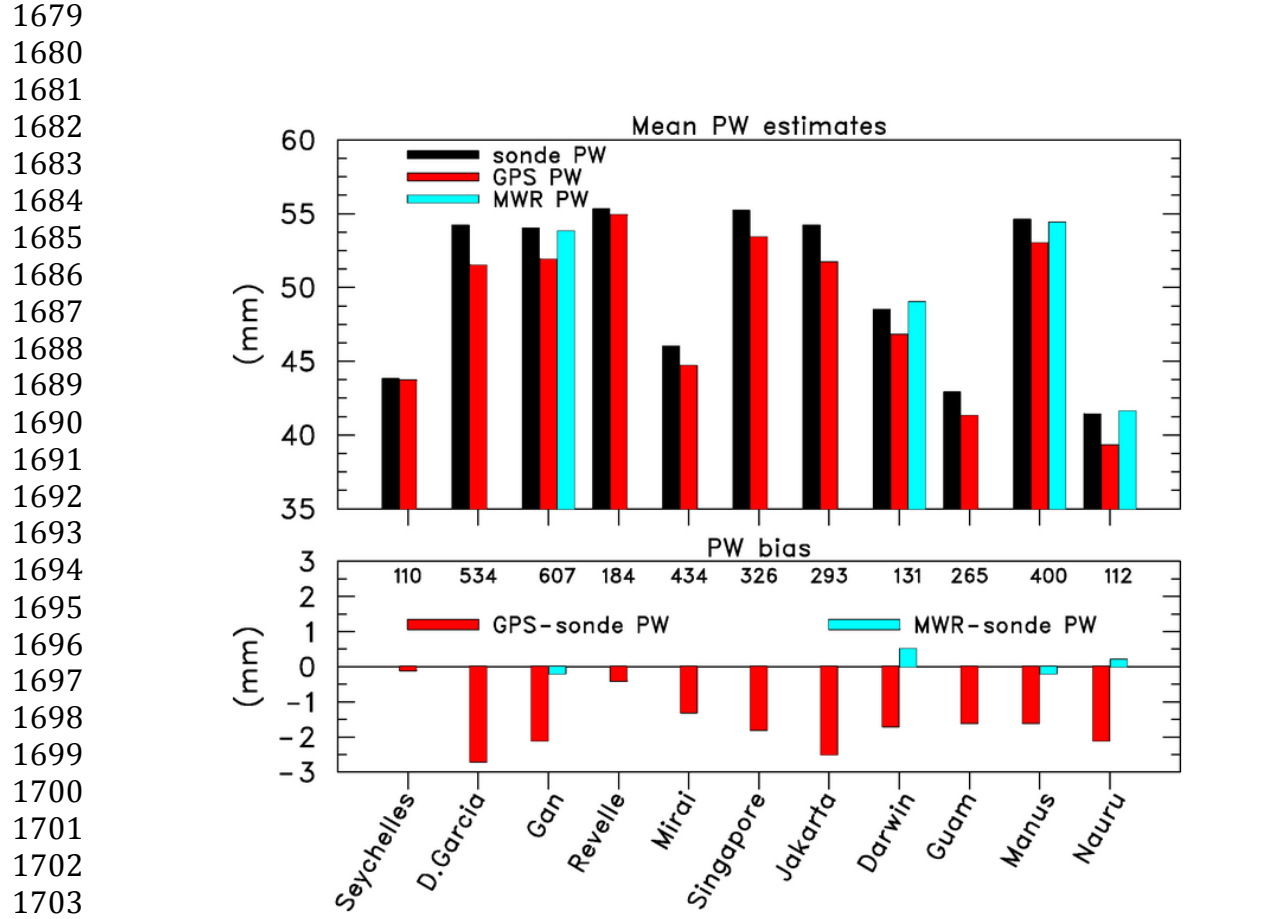


FIG. 14. PW estimates for several sites in the DYNAMO domain, listed from west to east, from sonde (black bar), GPS (red bar) and MWR (cyan bar). (Top) shows mean for times when all estimates at a given site were available during EOP. (Bottom) shows PW bias defined as independent PW estimate minus sonde estimate. Numbers along top of panel indicate the number of comparisons that went into means.

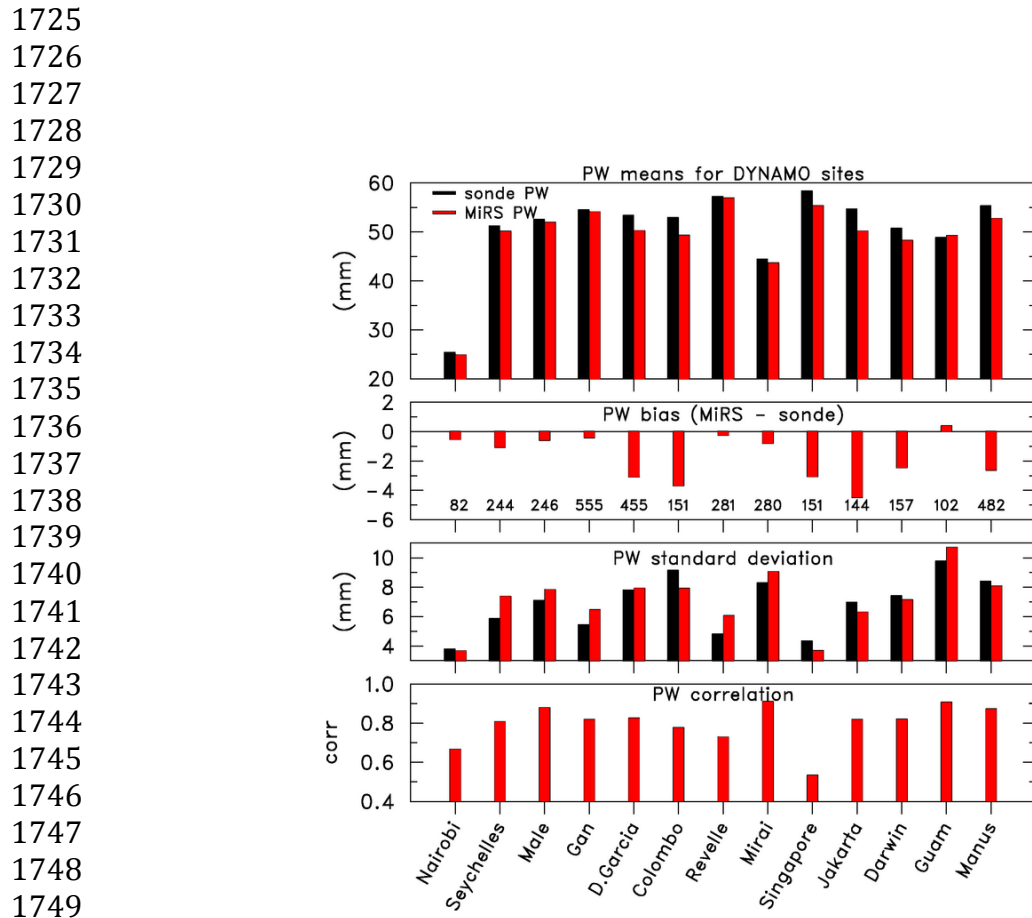


FIG. 15 Comparison of sonde PW statistics to MiRS PW (sonde– black bars, MiRS – red bars) for 13 DYNAMO sites listed from west to east for period 1 October to 31 December 2011. (from top to bottom) PW means, PW difference where negative values imply a MiRS dry bias, PW standard deviations, temporal correlation coefficient of sonde PW estimates to MiRS product.

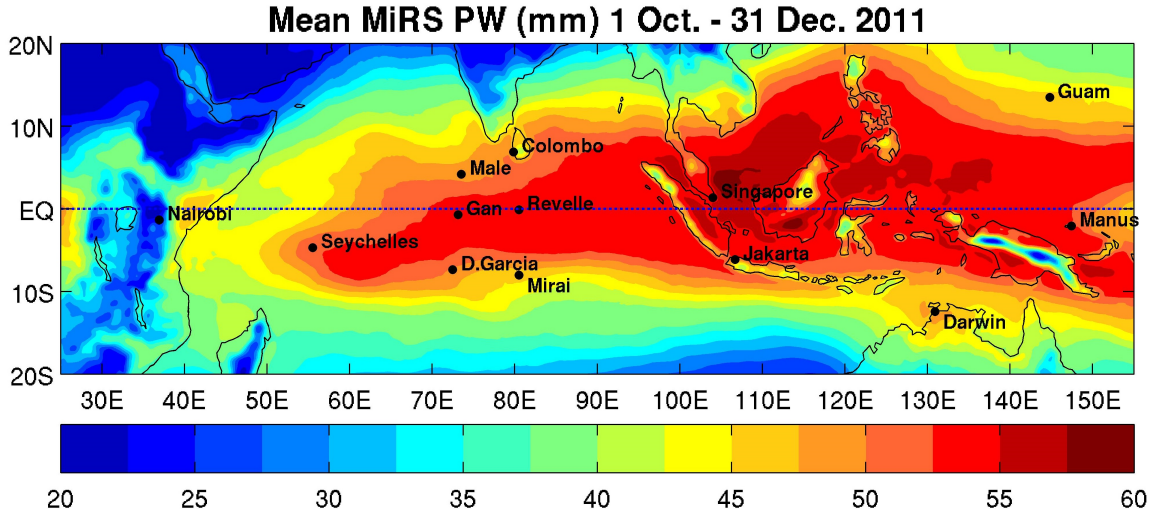


FIG. 16. Mean PW map based on MiRS analyses for period 1 October to 31 December 2011. Location of DYNAMO sounding sites examined in Fig. 15 are shown on map. Color scale at bottom is in mm.

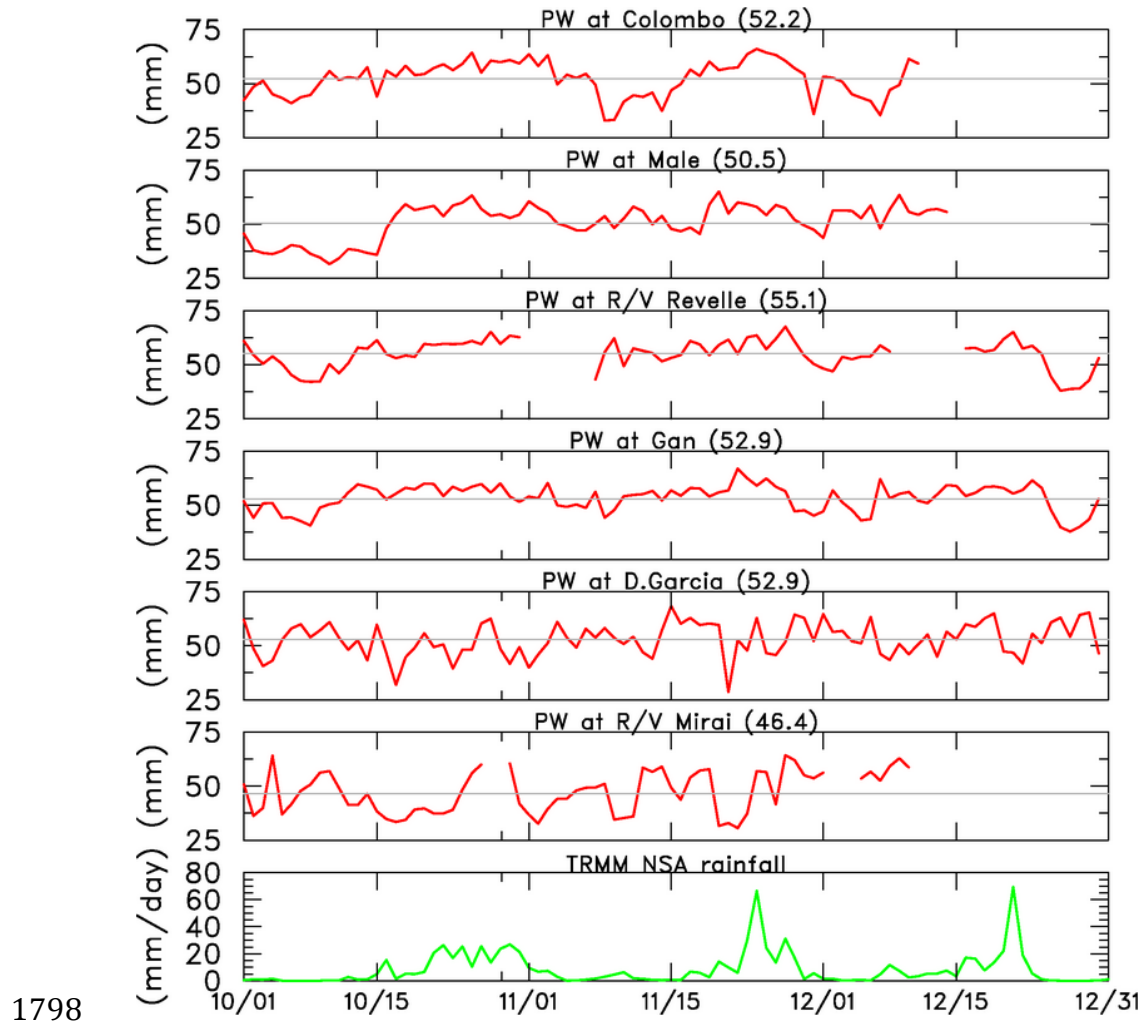
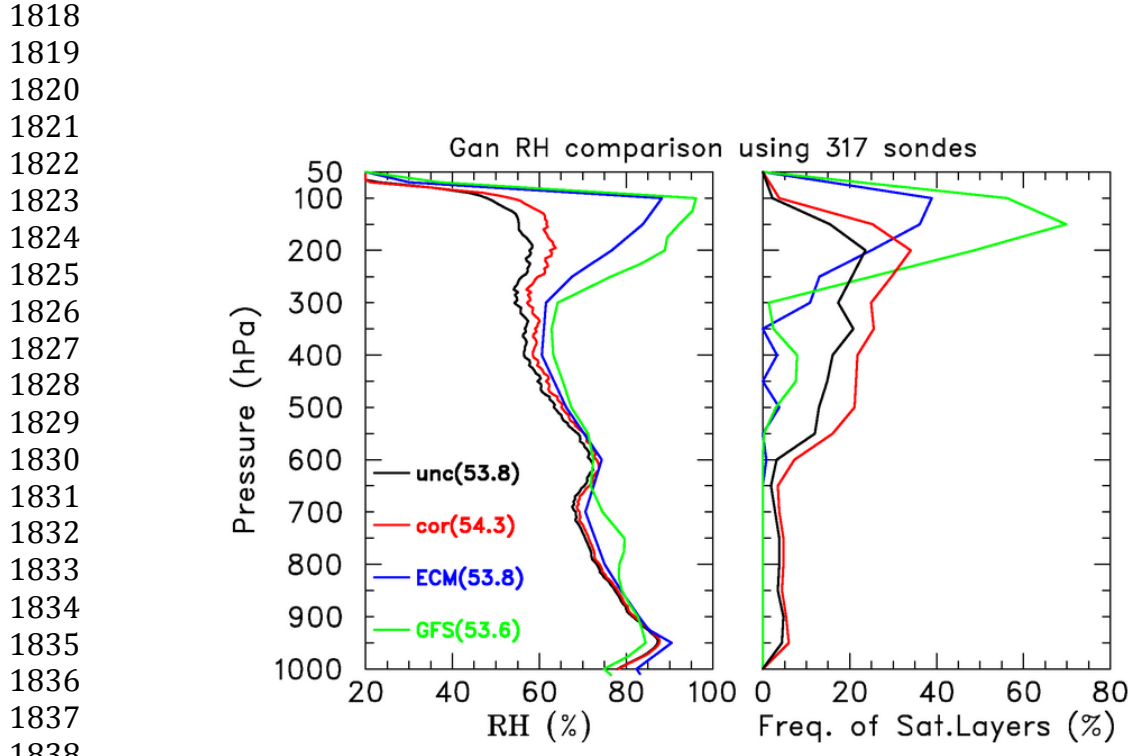


FIG. 17. Daily averaged PW time series for 6 core sites and (bottom) TRMM 3B42 rainfall averaged over the NSA. Mean PW is shown by thin gray line and is listed in parentheses.



1864
1865
1866
1867
1868
1869
1870
1871
1872
1873
1874
1875
1876
1877
1878
1879
1880
1881
1882
1883
1884
1885
1886
1887
1888
1889
1890
1891
1892
1893
1894
1895
1896
1897
1898
1899
1900
1901
1902
1903
1904
1905
1906
1907
1908
1909

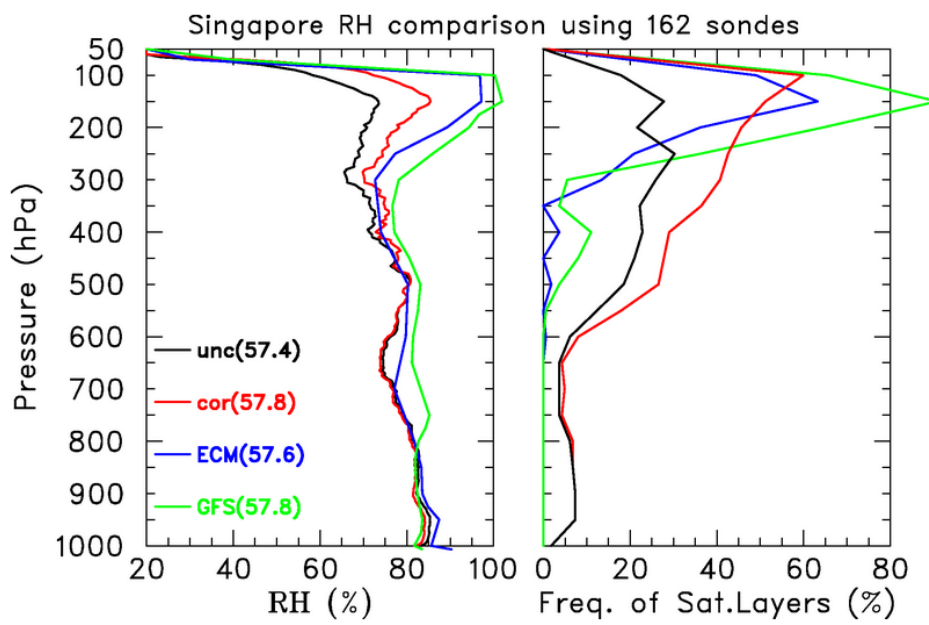


FIG. 19. As in Fig. 18, except at Singapore for period 1 October to 21 December. Here VRS92 sonde humidity was corrected using NRBC algorithm.

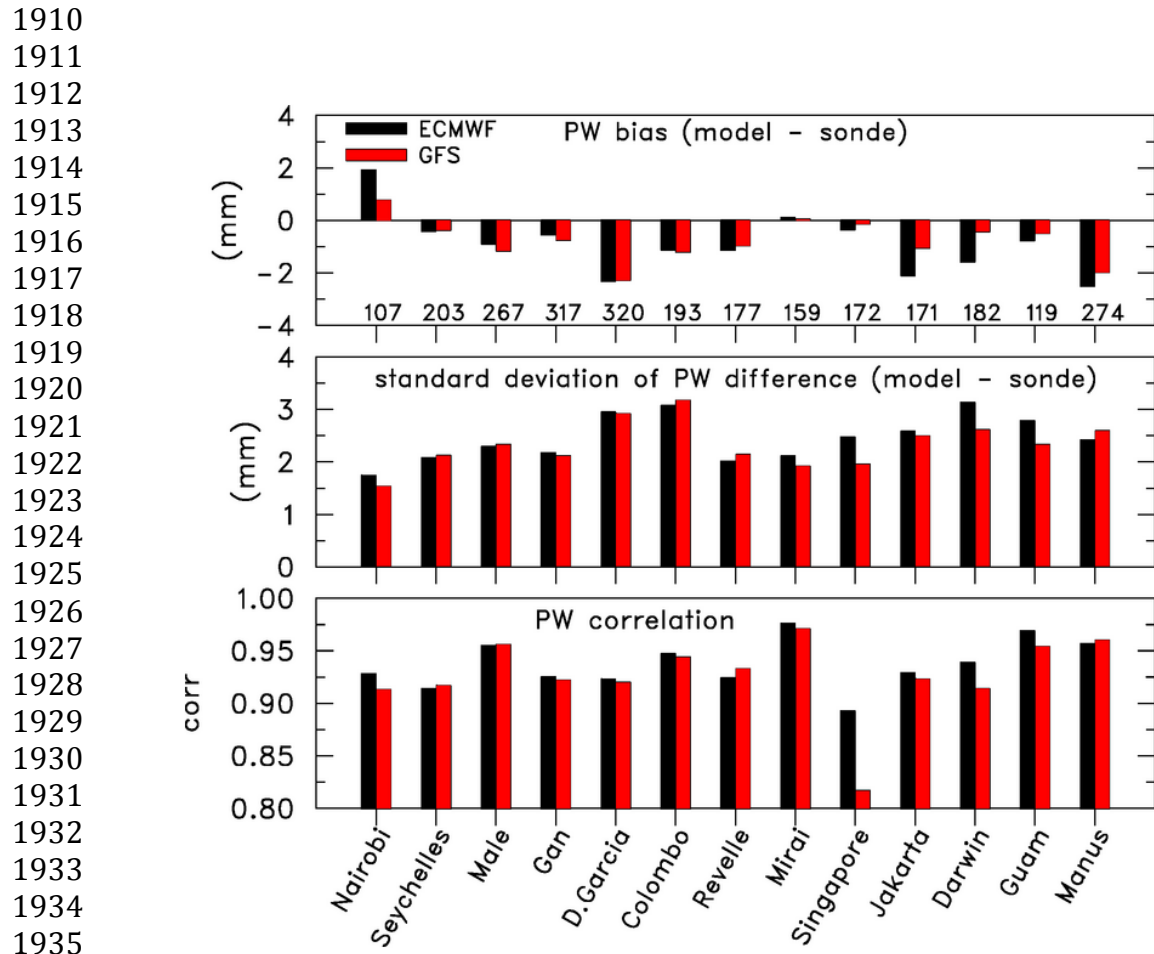


FIG. 20. Comparison of sonde PW statistics to OA PW (ECMWF – black bars, GFS – red bars) for 13 DYNAMO sites listed from west to east for period 1 October to 31 December 2011. (top) Difference in PW means (model – sonde) where negative values imply a model dry bias, (middle) standard deviation of PW difference, (bottom) temporal correlation coefficient of sonde PW estimates to OA products.